Master's Thesis

Synthesis and Characterization of Paintable Bi_2Te_3-based Thermoelectric Materials

Sung Hoon Park

Department of Materials Science and Engineering

Graduate School of UNIST

2017

Synthesis and Characterization of

Paintable Bi_2Te_3-based Thermoelectric Materials

Sung Hoon Park

Department of Materials Science and Engineering

Graduate School of UNIST

Synthesis and Characterization of

Paintable Bi_2Te_3-based Thermoelectric Materials

A thesis
submitted to the Graduate School of UNIST
in partial fulfillment of the
requirements for the degree of
Master of Science

Sung Hoon Park

15. 12. 2016
Approved by

Advisor
Jae Sung Son

Synthesis and Characterization of

Paintable Bi_2Te_3-based Thermoelectric Materials

Sung Hoon Park

This certifies that the thesis of Sung Hoon Park is approved.

12/15/2016 of submission

Advisor: Jae Sung Son

Wook Jo

Kyoung Jin Choi

Abstract

Synthesis and Characterization of Paintable Bi_2Te_3-based Thermoelectric Materials

Sung Hoon Park

School of Materials Science and Engineering

The Graduate School

Ulsan National Institute of Science and Technology

The thermoelectric (TE) effect has attracted considerable attention from a number of different research areas, as its ability to directly convert between thermal and electrical energy offers a unique solution for sustainable power generation from waste heat sources. The power generation performance of solid-state TE devices largely depends on the characteristics of the TE materials from which they are made, such as the energy conversion efficiency. This efficiency is estimated from a dimensionless figure-of-merit: $ZT = (S^2\sigma T/\kappa)$, where S, σ, κ, and T are the Seebeck coefficient, electrical conductivity, thermal conductivity, and temperature, respectively. The shape and dimensions of TE materials are also crucial to efficient energy conversion in system-level TE modules with minimum heat loss. Typically, TE legs chipped into planar-structured TE devices are fabricated by means of a top-down dicing process to produce cube or cuboid-shaped TE blocks, in which TE ingots are synthesized through energy intensive processes such as zone-melting or hot-pressing. Although these conventional technologies can produce bulk-scale TE legs with well-established TE properties and moderately high ZT values, a key constraint lies in the difficulty in engineering the shapes and dimensions of the TE legs. This restricts the flexibility in designing TE devices for efficient thermal energy transfer from heat sources with various shapes. A few attempts have been made to design and fabricate ring-shaped TE legs chipped into tubular TE devices for energy harvesting from exhaust pipes, but achieving suitable performance and process simplicity remains a challenge. This dissertation describes the synthesis and characterization of Bi_2Te_3-based TE paints. In particular, the bulk-level TE properties of the painted materials are reported. In

addition, the power generating performance of TE devices fabricated on curved heat sources via the painting process is discussed.

First, the background of TE research area is briefly described. The basic principles of TE phenomenon such as the Seebeck effect, the Peltier effect, and the Thompson effect are described. Furthermore, the structural and TE characteristics of Bi_2Te_3-based TE materials, arguably the best TE materials at near room temperature are discussed. Finally, the measurement methods of TE devices and their types are described.

Second, it has been described that the Bi_2Te_3-based TE paints aided by Sb_2Te_3-based molecular chalcogenidometalate (ChaM) are synthesized and their TE properties are characterized. ChaM ions are known for soluble precursor and widely utilized these molecules as inorganic ligands and solders for nano- and meso-scale semiconductor particles, and so I simply expand this concept to TE paints. Molecular Sb_2Te_3 based ChaM is used as a solder or a sintering aid for n-type BiTeSe and p-type BiSbTe TE particles. The Sb_2Te_3-ChaM easily fills the voids and interfaces between these TE particles, forming interconnecting crystalline phases without the need for external pressure. The soldering effect substantially influence TE properties of the painted materials, of which *ZT* values increase up to 1.21 and 0.69 for p-and n-type materials. Furthermore, the fabricated in-plane TE power generators via the painting process exhibits remarkably high output power density of 4.0 mW/cm^2 under the temperature difference of 50 ^oC. In particular, the thourgh-plane TE power generator chipped with the molded TE blocks shows ~30 mW/cm^2 under the temperature difference of 50 ^oC, competing the commercial planar-structured TE module. This painting approach therefore provides a simple and cost-effective way to design and fabricate TE devices directly onto any shaped heat source using a brush, thereby eliminating the need for additional equipment. What makes this painting process suitable for preparing TE devices is the fact that they are less sensitive to the resolution of the mm-scale TE legs than other electronic devices.

Contents

List of Figures

Chapter 1. Introduction

1.1 Back ground of thermoelectric phenomenon

1.1.1 The Seebeck effect

Thermoelectric (TE) effect was discovered by German Physicist Thomas Johann Seebeck in 1821. T.J. Seebeck formed a closed circuit with hetero-materials which consist of Bi /Sb or Cu/ Bi. He found unusual phenomenon when the heat was applied to one side of the circuit, the needle of a compass deviated from the north and south orientation due to polarization of conductors. The Seebeck effect generates TE power when there is a temperature difference between the junctions of different kinds of materials. (Figure 1.1a) In other words, the ratio of generated voltage(V) and temperature(T) gradient is called the Seebeck coefficient(S).

$$S = {}^{dV}/_{dT} \tag{1.1}$$

A typical example of applying the principle of Seebeck effect is a thermocouple formed by joining materials that have different Seebeck coefficients. These thermocouples have a variety of Seebeck coefficients depending on the temperature, and they are very useful for measuring temperature. At the atomic scale, when TE material is heated, the charge carriers spread to the cold side which leads to the production of electrostatic potential energy due to the accumulation of charge carriers at the cold end[2]. (Figure 1.1b)

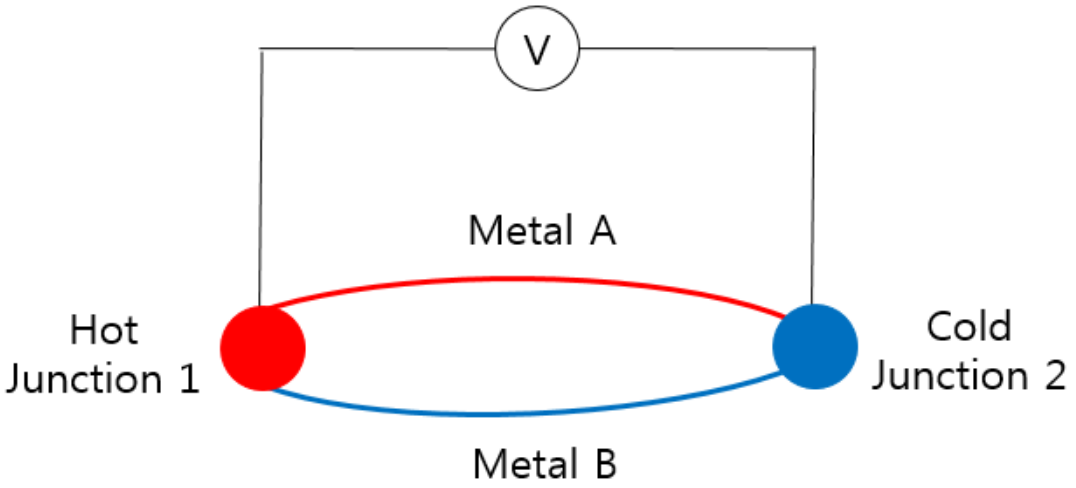

(a)

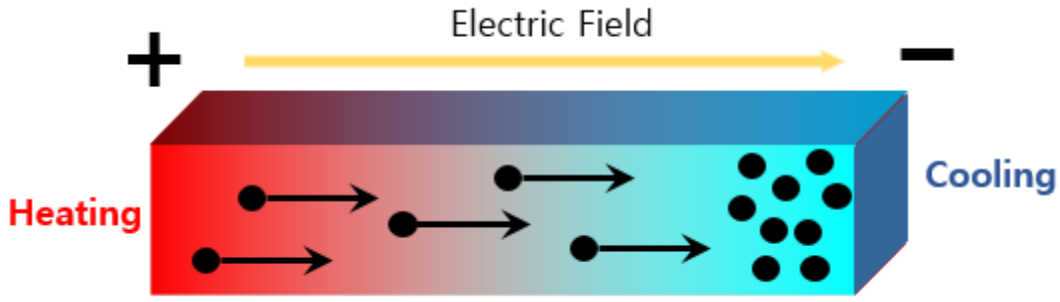

(b)

Fig. 1.1. Basic principle of Seebeck effect in TE materials.

1.1.2 The Peltier effect

Peltier effect is the creation of endothermal and exothermal reaction when the current is flowed to the junction of hetero-materials[1]. This effect is named after Jean Charles Peltier who first observed it in 1834. When the current is applied in a reverse direction, the endothermal and exothermal reaction occurs in reverse at the junction. Peltier effect is thermodynamically reversible and is also inverse of Seebeck effect. The Peltier coefficient (Π) is defined as the ratio of heat flow (Q) to current flow (I).

$$\Pi = {}^{Q}/_{I} \tag{1.2}$$

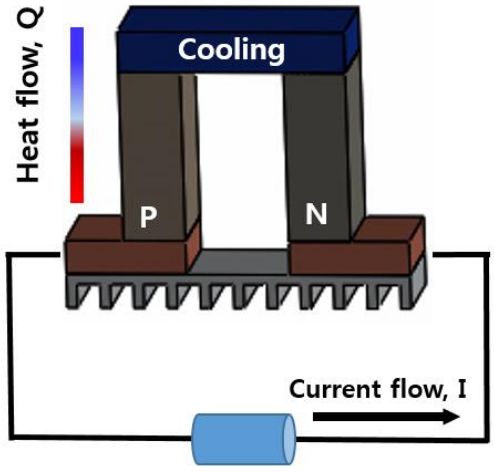

Fig. 1.2. Schematic illustration of the Peltier effect.

The band diagram of charge carrier mechanism in using semiconductor is shown in Figure 1.3. When the heat is transported along the direction of the charge carrier, the charge carrier needs enough energy as much as the gap of metal and semiconductors to move to the valance band (hole) or conduction band (electron).

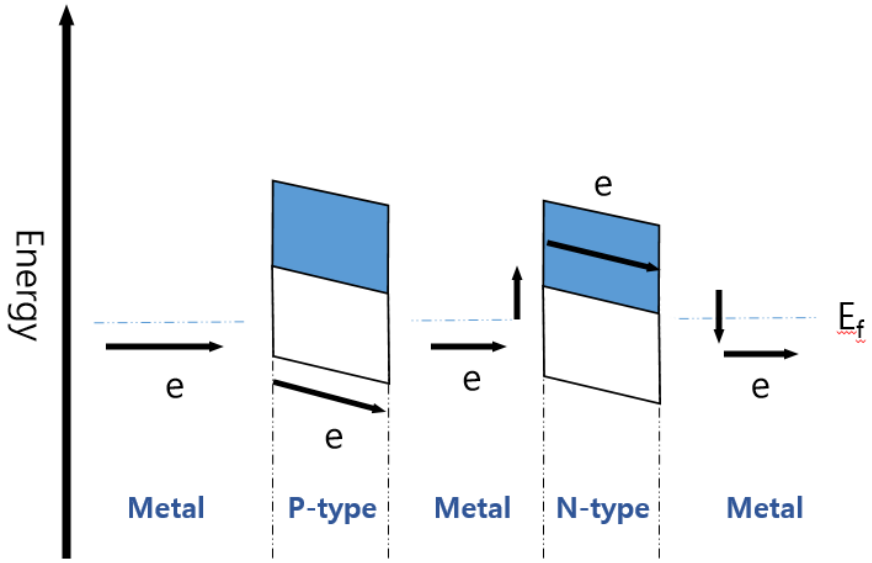

Fig. 1.3. band diagram for Peltier effect.

1.1.3 The Thomson Effect

When the current is applied to TE material, generating of heat reactions are called Thomson Effect. If a current is passed through a conducting material, heat production per unit volume is

$$q = -\rho J^2 \tau I \Delta T \tag{1.3}$$

Where ρ is the resistivity, I is current density, ΔT is temperature difference at both end of material, τ is the Thomson coefficient. The term of $\tau I \Delta T$ means Thomson heat and ρJ^2 imply Joule heating effect.

Fig. 1.4. Schematic illustration of the Thomson effect.

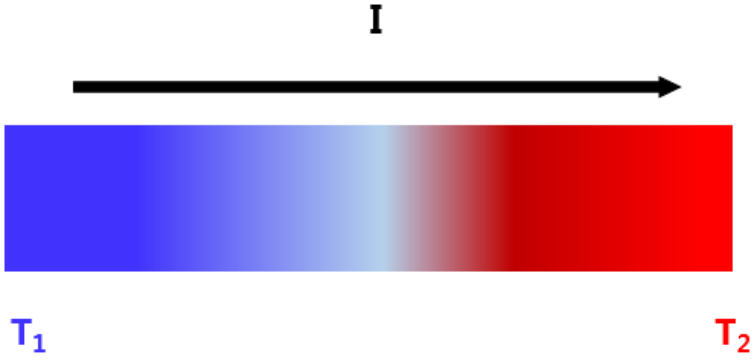

1.1.4 Evaluation of thermoelectric materials

The performance of TE materials (ZT = dimensionless figure of merit) is generally defined by calculating Seebeck coefficient (S), electrical conductivity (σ), thermal conductivity (K), and operation temperature. The equation of ZT is shown in equation 1.4.

$$ZT = \frac{S^2\sigma}{k}T \tag{1.4}$$

$S^2\sigma$ is typically called a power factor (PF). The ZT values is proportional to the square of Seebeck coefficient and electrical conductivity and is inversely proportional to the thermal conductivity. High Seebeck coefficient and electrical conductivity is essential for the maximum TE power and to minimize the energy leakage. The thermal conductivity must be low to keep the temperature gradient. The equation is in dimensionless form that is multiplied by the operation temperature because all parameters vary with the operation temperature.

It is very difficult to enhance ZT property since the TE performance has a trade-off relationship among TE properties. For degenerate semiconductor, Seebeck coefficient (S) can be expressed by Mott expression[4]

$$S = \frac{\pi^2 k^2 m^* T}{3eh^2}\left(\frac{\pi}{3n}\right)^{\frac{2}{3}} \tag{1.5}$$

, where λ, k, T, m*, e, h, and n are the scattering parameter, Boltzmann's constant, absolute temperature, effective mass, electronic charge, Planck's constant and carrier concentration. The electrical conductivity (σ) express by following equation.

$$\sigma = \frac{1}{\rho} = ne\mu \tag{1.6}$$

, where ρ, and μ are the electrical resistivity and mobility.

As shown in equation 1.5, the S is proportional to m* and inversely is proportional to n. Also, as represented in equation 1.6, the σ is proportional to n and μ that lead to trade off relationship of S and σ. The thermal conductivity (k) comes from two parts which consist of electron and phonon components. (1.7) The electron term is related to the σ through the Wiedemann-Franz law. (1.8)

$$k = k_{el} + k_{\mathrm{ph}} \tag{1.7}$$

$$k_{el} = L\sigma T \tag{1.8}$$

, where k_{el}, k_{ph} and L is the Lorenz factor. (2.4 X $10^{-8}J^2K^{-2}C^{-2}$ for free electron)

According to the Wiedemann-Franz law, it is impossible to independently control the electron contribution of thermal conductivity and electrical conductivity. However, the phonon contribution of thermal conductivity could be controlled by introducing the molecular nano-sized particles into microparticles which are under tens of nanometer in scale[5].

The figure 1.5 shows interrelationship about the conflicted terms of TE properties depending on carrier

concentration which can be easily varied by the addition of dopant concentration and the exchange the polarity by added the doping type. If the carrier concentration is low, it has high thermopower but it shows extremely low electrical conductivity and thermal conductivity similar to that of an insulator and if the carrier concentration is high, it shows considerably low seebeck coefficient and have high thermal conductivity similar to that of a metal.

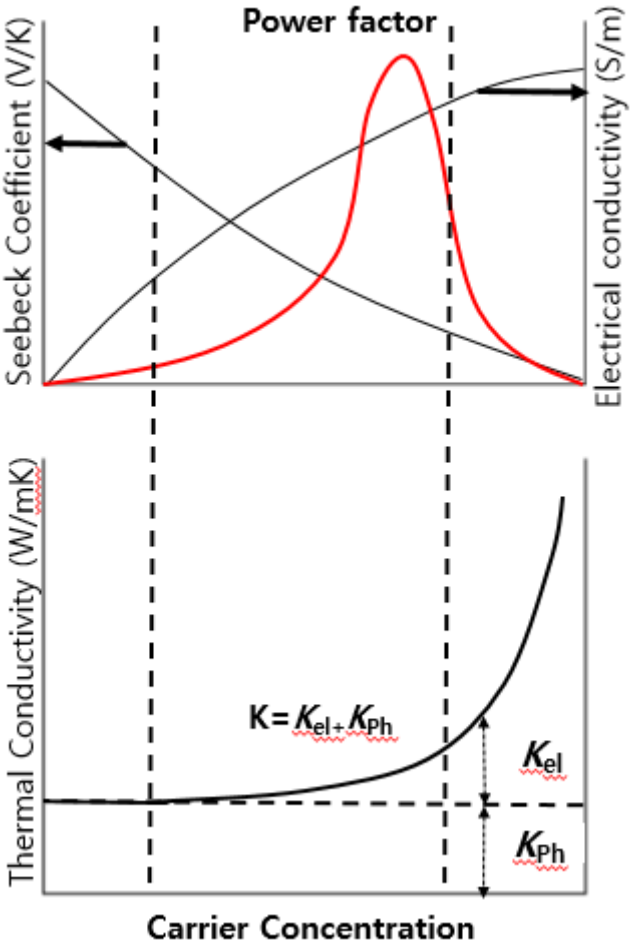

Fig. 1.5. Interrelation of the TE properties.

1.2 Thermoelectric materials

The most widely used TE materials for generator or refrigerator near room temperatures (~200℃) is bismuth telluride based alloys. Bi_2Te_3 material have been proved to alloy easily with Sb_2Te_3, and Sb_2Se_3 enables to adjust the carrier concentration and reduces lattice thermal conductivity. Up to date, Bi_2Te_3 based n- and p-type TE material provide us with reliable energy source as generator or cooling device. Group-Ⅳ tellurides (PbTe, GeTe and SnTe) materials are typically used in mid-temperature TE system.

Also, the figure of merit of $AgSbTe_2$-based materials indicated above the ZT=1. For high temperature (600℃~) TE generator, SiGe alloys have been utilized for n- and p-type TE materials[2].

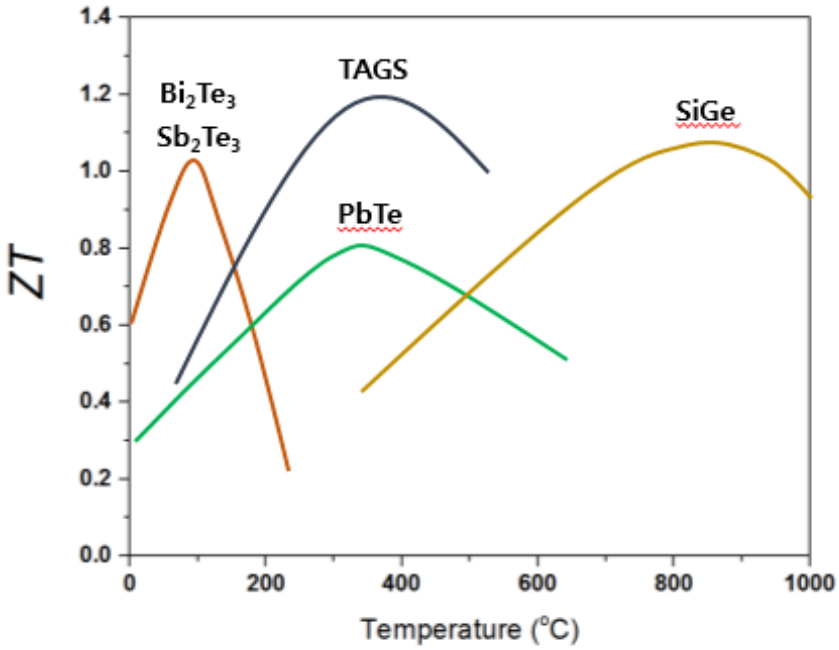

Fig. 1.6. State of the art TE materials depending on temperature.

1.2.1 Characteristic of Bismuth-Telluride material

The crystal structure of Bi_2Te_3 material is shown Figure. 1.7.

$$-Te^{(1)}-Bi-Te^{(2)}-Bi-Te^{(1)}-$$

Above five-layer structure is named a quintet in which the rhombohedral structure consists of three quintets. The layer of $-Te^{(1)}-Bi-$ and $-Bi-Te^{(2)}-$ are held together by strong ionic-covalent bonds and covalent bonds while the $-Te^{(1)}-Te^{(1)}-$ layer is held by Van Der Waals bond[6]. The mechanical strength of Bi_2Te_3 is very weak due to the existence of cleavage along the basal plane perpendicular to the c-axis. Therefore, the mechanical strength and the transport properties of Bi_2Te_3 based TE materials have a strong anisotropy[7].

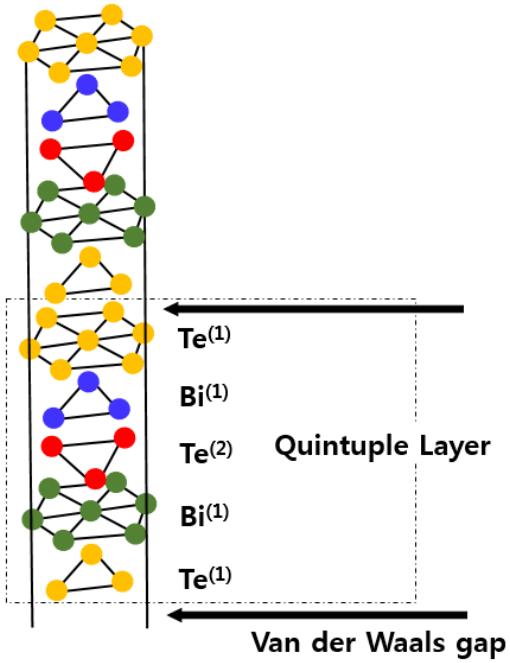

Fig. 1.7. Crystal structure of bismuth telluride.

The band structure of Bi_2Te_3 has been proved to have several-valley model. This material has an indirect band gap of 0.13 eV at 300 K[8].

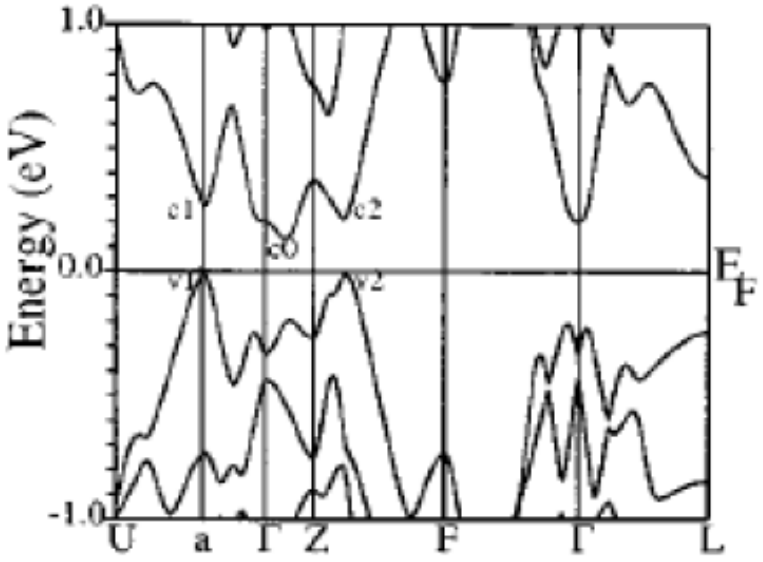

Fig. 1.8. Band structure of bismuth telluride.
The figure is reproduced with permission from Ref. [8], APS.

The $(Bi_{1-x}Sb_x)_2Te_3$ is p-type TE materials which is formed by adding the Sb_2Te_3 to Bi_2Te_3 and $Bi_2(Te_{1-x}Se_x)_3$ solid solutions are constituted from n-type Bi_2Te_3 and Bi_2Se_3. Those compounds are all same rhombohedral structure with Van der Waals bonding. Generally, excess of Bi or Sb exist in $(Bi_{1-x}Sb_x)_2Te_3$ solid solution due to Te evaporation[9]. The $Te^{(2)}$ place is occupied by Bi or Sb atoms that result in anti-site defect which make p-type materials by forming each five excess Bi or Sb in three hole. The $Bi_2(Te_{1-x}Se_x)_3$ solid solutions are produced by substituting Te atoms with Se. At first, the Se atoms occupy the $Te^{(2)}$ atoms and the $Te^{(1)}$ places are filled with Se atoms. Because Se is more electronegative than Te, the bad gap increases to 0.31eV for x=0.3[ref. 10]. The defect equilibrium equations of Bi_2Te_3, Sb_2Te_3, Bi_2Se_3 are presented below

$$Bi_2Te_3 = 2Bi_{Te'} + V_{Te} + 2V_{Bi} + (3/2)Te_{2(g)} + 2h$$
$$Sb_2Te_3 = 2SbTe' + V_{Te} + 2V_{Sb} + (3/2)Te_{2(g)} + 2h \quad (1.9)$$
$$3Bi_2Te_3 = 4Bi_{Bi} + 2Bi_{Se'} + 7V_{Se} + 2V^{1.5}_{Bi'} + (9/2)Se2(g) + 2e$$

Based on the above equation[11,12], the TE properties are presented with carrier type and concentration.

1.2.2 The strategies to enhance the *ZT* value

Until now, the efficiency of TE bulk materials have been indicated ZT=1. As aforementioned, finding a proper carrier concentration and new method to decrease thermal conductivity is essential to produce the maximum power factor. In the mid-1990s, the Slack insisted well-established concept referred as the "phonon glass electron crystal" (PGEC)[13]. It means that a structure has a low $K_{lattice}$ similar to a glass and simultaneously a crystal-like high electrical conductivity. The crystal structure of the PGEC materials show a large cage-like empty space which has massive atoms (rattling atoms) that result in a phonon damping effect that can extremely reduce the lattice thermal conductivity. Also, this crystal structure coexists with charge carrier of high mobility.

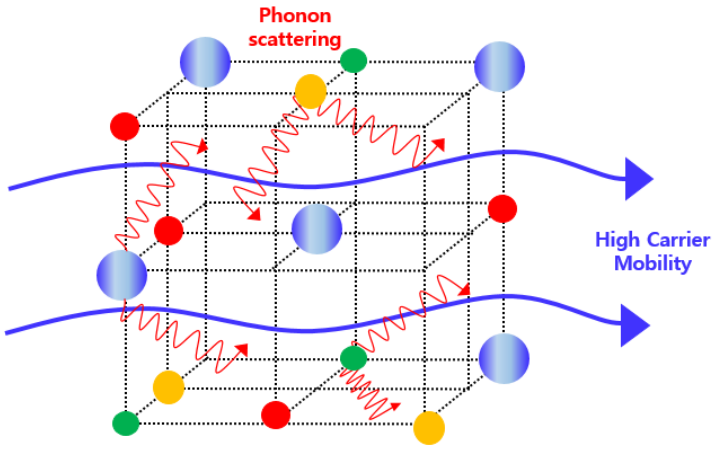

Fig. 1.9. The Schematic illustration of PGEC concept

The representative example with a PGEC structure is skutterudites[14], clathrates[15], half-heusler[16], and metal oxide[17]. Skutterudites are $CoAs_3$-type compounds and their space group is cubic $Im\bar{3}$ with the general formula XY_3 (X= Co, Rh, Ir and Y=P, As, Sb). The $CoSb_3$ has been the most widely-studied material due to its high-power factor that originates form the high weighted carrier mobility. The clathrates are generally low-thermal conductivity compounds with open frameworks composed of tetrahedrally coordinate Al, Ga, Si, Ge, or Sn. The framework has cages that can incorporates large electropositive atoms. Half-Heusler is a combination of a rocksalt-type and a zincblende-type crystal structure which consists of three filled interpenetrating FCC sub-lattices and one vacant sub-lattice. The general formula is XYZ, where X and Y are transition metals and Z is a main-group element[18].

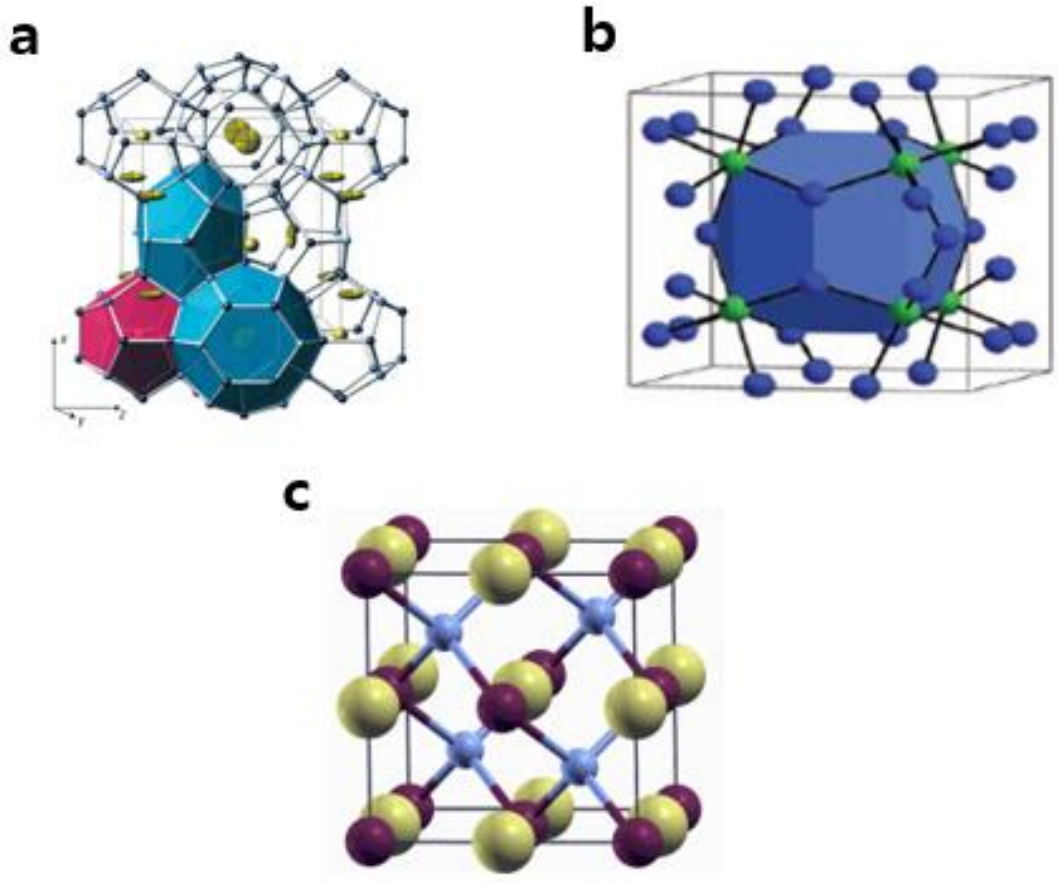

Fig. 1.10. The examples of PGEC crystal structure (a) clathrates, (b) skutterudites, (c) half-heusler. The figure is reproduced with permission from Ref. [2,15,16], AAAS, NPG and RSC.

Other ideas to increase TE efficiency is using low dimensionality. In 1993, Dresselhaus implemented a theoretical analysis on enhanced Seebeck coefficient for quantum wires and wells[19,20]. The high electronic density of state(DOS) near E_F due to quantum confinement effects from low-dimensional

materials lead to increase the seebeck coefficient.

Based on the Mott equation (1.10), The Figure 1.11 indicated the quickly changing DOS is needed to achieve the high Seebeck coefficent . This theory has been demonstrated experimentally in quantum dots, quantum wire and quantum well[21].

$$S \approx \frac{d\ln\sigma(E)}{dE}\Big|_{E=E_f} \tag{1.10}$$

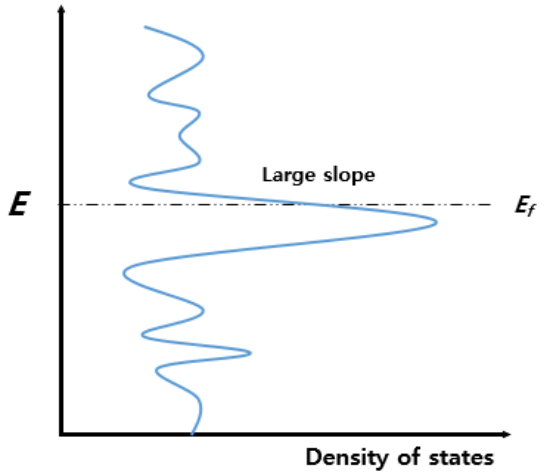

Fig. 1.11. Hypothetical DOS with a large slope.

Another approach to increase the *ZT* is energy filtering effect. When the metallic material introduces into host semiconductor materials, it produces the potential wall which confined the low energy carrier. So the only high energy carrier go by the interface without disturbance that lead to increase for Seebeck coefficient. The relationship between of energy and relaxation times (τ) can be described as $\tau \approx \tau_0 E^r$, where the *r* is called the scattering parameter. Increase of the slope of the differential conductivity is from the increase of *r* and therefore increasing the Seebeck coefficient.

The resonant doping is also a potential method for improving Seebeck coefficient. By introducing resonant impurity level into the conduction or valence band, sharp features in the DOS is created by the resonant states. Heremans *et al.* experimentally demonstrates the concept of the resonant doping in bulk TI-doped PbTe[22].

Nowadays, many scientists focus on reducing the thermal conductivity through the diverse nanostructuring approaches. By introducing nanoscale structure, preferential scattering is possible because the mean free paths (MFP) of phonons is much bigger than MFP of carrier. So, it enables to selectively scatter the phonon at grain boundary if the dimension or size of particles were properly

controlled and therefore the thermal conductivity significantly decreases without affecting the electronic transport properties. The most notable experiment to support this theory is conducted by Poudel[23]. He synthesized the polycrystalline p-type TE bulk alloy using hot press method of mechanically alloyed nanoscale powders and the morphology was thoroughly examined. This material exhibited a *ZT* of 1.2 at room temperature and impressive maximum *ZT* of 1.4 at 373 K due to reduction form K_l of 0.35–0.4 $Wm^{-1}K^{-1}$. The isotropic *ZT* resulted from the random grain orientation of the sample. Although the electrical conductivity was reduced at some extent, the thermal conductivity was reduced more significantly from the bulk ingot of the same material. The figure 1.13 shows SEM images of bulk p-type TE materials with the nanoscale grain, crystallinity, random orientation

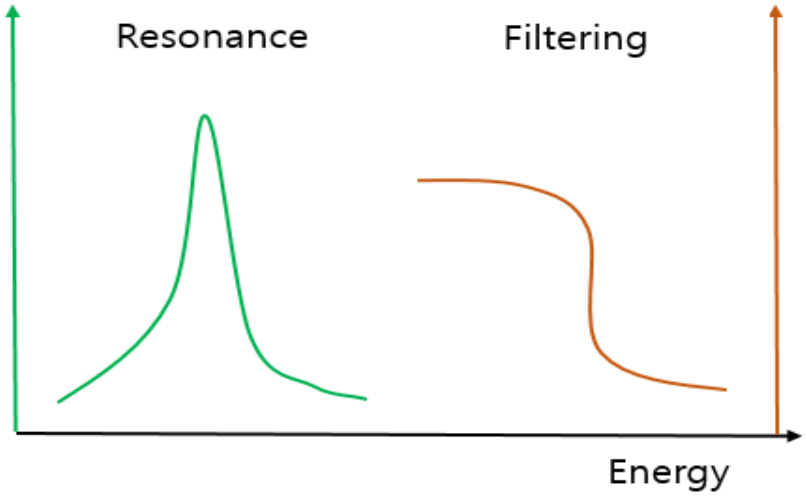

Fig. 1.12. The effect of resonant doping and energy filtering effect depend on energy.

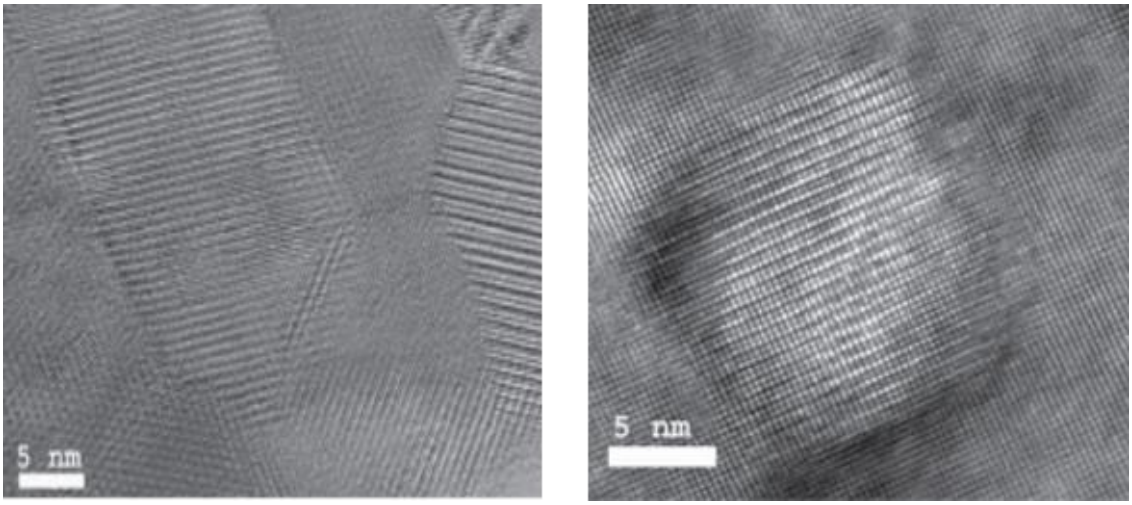

Fig. 1.13. The SEM image of (left side) nano-grain boundaries and nano-precipitate (right side). The figure is reproduced with permission from Ref. [23], AAAS.

Melt spinning followed by spark plasma sintering process produced bulk amorphous nanocrystalline precipitates leading to significantly low thermal conductivity. Kim. *et.al*, produced the high performance *ZT* (p-type) of 1.86 at 46.85 °C from full-spectrum phonon scattering through the dense dislocation arrays formed at low-energy grain boundaries by liquid-phase compaction in $Bi_{0.5}Sb_{1.5}Te_3$ which effectively scatter mid-frequency phonons together with low-and high-frequency phonons originated form grain boundary and point-defect scattering[24]. Further enhancement of *ZT* of p-type TE material may be possible through the grain boundary engineering such as combination of nanograined bulk, nanoinclusion, high density grain boundary and hetero-nanograined composite

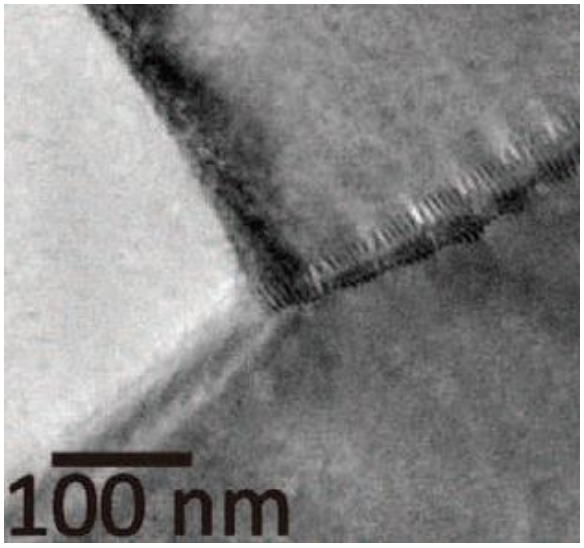

Fig. 1.14. The TEM image of dislocation arrays embedded on grain boundaries
The figure is reproduced with permission from Ref. [24], AAAS.

The n-type TE materials have completely different mechanism compared with those of p-type. Typically, nanostructuring strategy works well with p-type TE polycrystalline materials. However, the performance of n-type TE materials is still low because anisotropy ratio of those materials is about twice as higher than p-type counterparts which would reduce PF rather than K_l[25]. Several methods have been attempted to improve the performance of n-type TE materials through controlling the number of the operations with hot-press or spark plasma sintering. For example, adjusting the formation energy of point defects for donor-like effects by hot deforming[26], texturing with optimal cupper doped nanocomposite lead to good reproducibility[27] and broad wavelength phonon scattering via tuning multiscale microstructure by hot deforming the commercial zone melting ingots directly[28]. Despite these efforts, the maximum *ZT* is still around at ~1.2 due to the innate feature of n-Type which tempers with making high efficiency materials. Find a new method is needed to overcome this issue

1.3 Thermoelectric device

1.3.1 Evaluation of thermoelectric device

Equation (1.11) shows the voltage of a TE generator without the load. It depends on the number of the thermocouples n, operating temperature difference ΔT, and Seebeck coefficient of the used pair of materials S_1(p-type), S_2(n-type)

$$V_{output} = n\Delta T(S_1 - S_2) \tag{1.11}$$

In general, the output power density (w, mW cm^{-2}) is calculated as:

$$w = I^2 mR = \frac{m\sigma S^2}{(1+m)^2 l}\Delta T^2 \tag{1.12}$$

, where I is the electric current, R is the internal resistance, σ is the electrical conductivity of the leg, m is the ratio of the internal resistance to the external load resistance, l is the length of the leg, ΔT is the temperature difference across the leg.[29] By matching the external load resistance to the internal resistance, this formulation is simplified to:

$$w = \frac{1}{4l} PF\Delta T^2 \tag{1.13}$$

, where PF is the power factor (σS^2) of the leg. Assuming the thermal equilibrium, the output power per density depends solely on two factors of PF and l.

On the other hand, one should note that the ΔT applied to the legs from a heat source strongly depends on the thermal conductivity (κ), l, and the thermal resistance (ψ) between the leg and a heat source: as shown in the following relation:

$$\frac{\Delta T}{(T_s - T_a)} = \frac{l}{l+\kappa(X+Y)} \tag{1.14}$$

, where $(T_s - T_a)$ is the overall temperature difference, and X and Y are the factors proportional to ψ at hot and cold sides. Under the same $(T_s - T_a)$, it is the higher ΔT across the leg that the longer l and lower κ cause[29]. Therefore, l dependence on the power output density has a trade-off relationship between R and ΔT, which requires the optimum l to maximize the highest power output density (Figure 1.15).

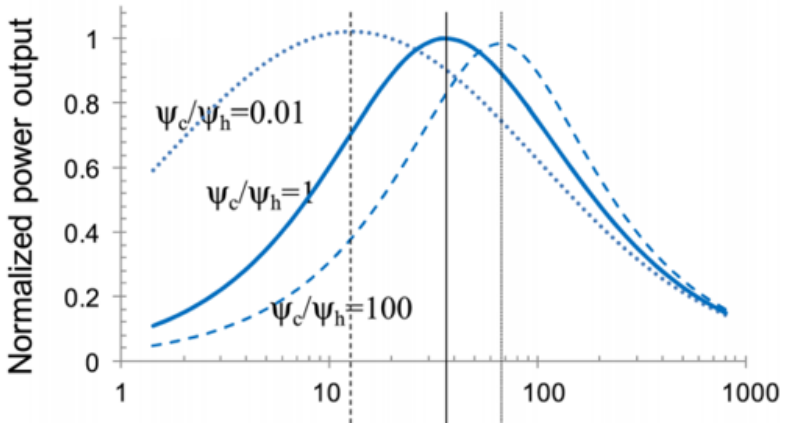

Figure 1.15. Power output normalized to the maximum as a function of normalized leg length (*x*-axis) with the assumption of T_a/T_s=0.1 and Z=1. The figure is reproduced with permission from Ref. [29], AIP.

1.3.2 Various types of thermoelectric materials and devices

Generally, the conventional TE device has a planar-structure with several n-and p-type legs in which would be limited when applied on to unevenly niche heat source. The flexible or wearable TE device stands out as a new type of devices that solves the problem. Therefore, it is essential to create the different form of conventional TE materials and processes such a screen printing, inkjet printing, lithography, vacuum deposition, CNT composites, PEDOT (3,4-ethylenedioxythiophene): PSS (polystyrene sulfonate), PANI and so on[30].

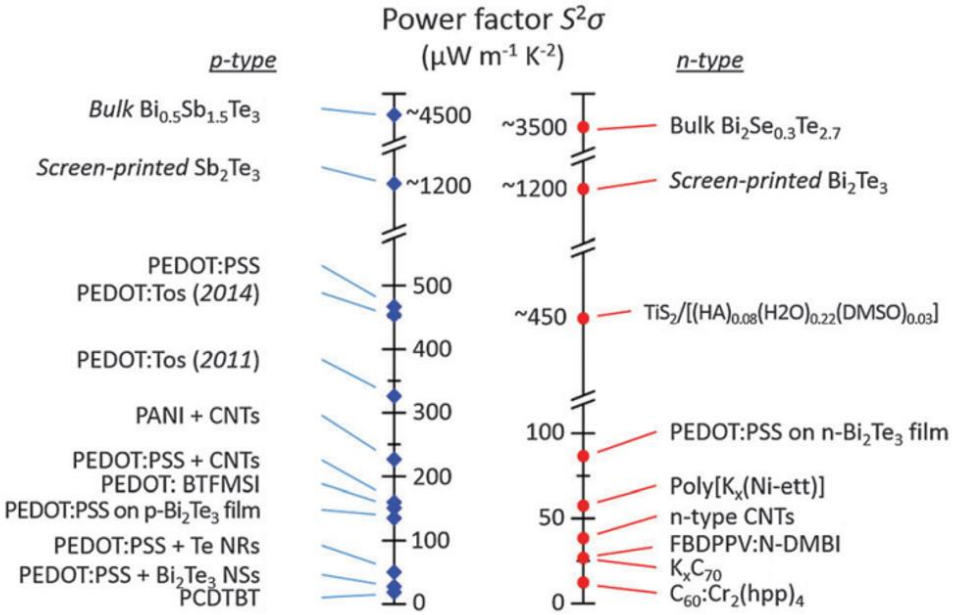

Figure 1.16. Power factor of various TE materials. The figure is reproduced with permission from Ref. [30], RSC.

The figure 1.17 shows the property of newly emerging TE materials as used screen printing process that indicated lower PF than bulk materials due to low electric conductivity which has glass fabric or polymer binder. Those additives were effectively used to bond the TE microparticles but the impurities also blocked the charge transport, leading to significantly reduce the electrical conductivity. For example, Varghese et al. synthesize nanocrystal inks using microwave-stimulated wet-chemical method followed by cold compaction and sintering which presents n-type films of a peak *ZT* of 0.43 together with the highest flexibility among the ink-type TE materials[31]. However, the electrical conductivity (about a 300 Scm^{-1}) and Seebeck coefficient (125 μV/K) are still lower than bulk. (Figure 1.16)

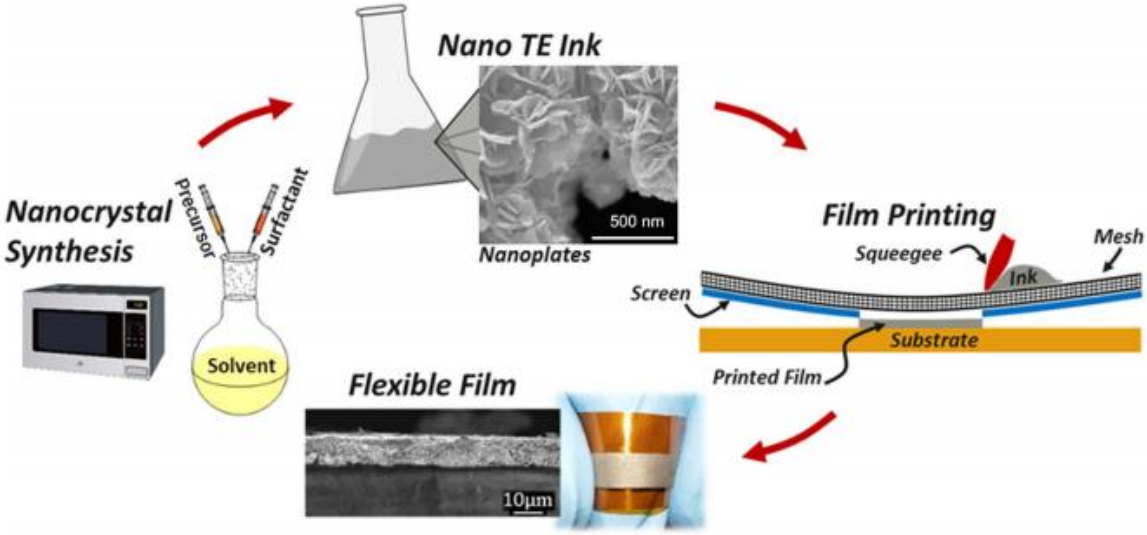

Figure 1.17. Schematic illustration of TE device fabrication via printing process. The figure is reproduced with permission from Ref. [31], NPG.

In other case, PEDOT: PSS is most widely used organic-based TE materials that has a good flexibility, stability air, and electrical conductivity. However, it shows one order lower PF compared to bulk material due to the Seebeck coefficient that has extremely low result from somewhat high carrier concentration. *Kim at al*. de-doped p-type PEDOT: PSS to reduce the counter ion volume by partially removing unionized counter ions that do not contribute to the charge density adversely reduced charge carrier mobility. Therefore, a high electrical conductivity and a reasonably high Seebeck coefficient were simultaneously achieved. These approach present *ZT* of 0.4 at room temperature that is highest value among the organic TE materials[32].

For aspect of device, the Kim et al. demonstrated the highest output power density of 3.8 mW cm^{-2} at temperature difference of 50 °C printing process using new device structure with a glass-fabric and a new electrode transfer technique. The material property of n-and p-type used in this work shows as low as *ZT* value of 0.35, 0.27. respectively[33].

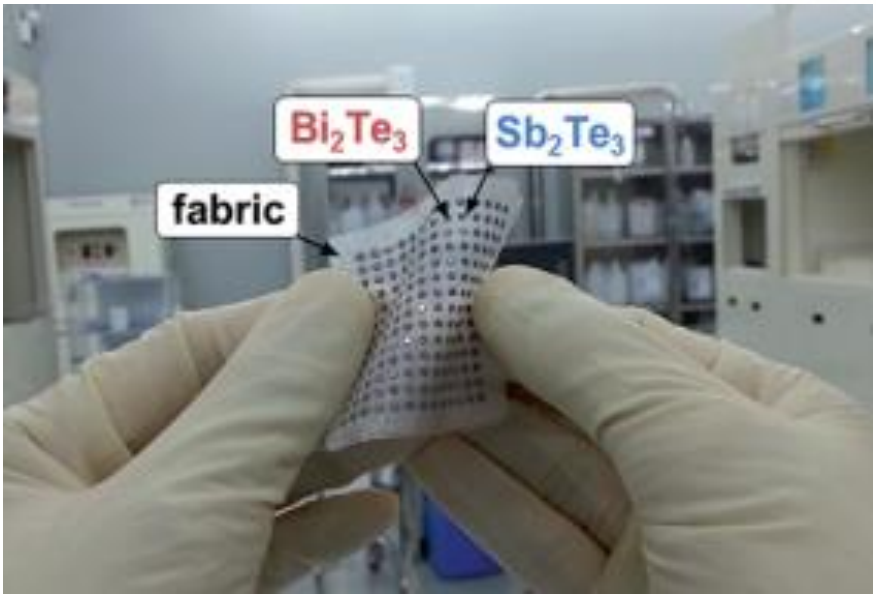

Figure 1.18 Photograph of Bi_2Te_3 and Sb_2Te_3 dots on a glass fabric of 40 mm X 40 mm. Power factor of various TE materials. The figure is reproduced with permission from Ref. [33], RSC.

So far, we have briefly reviewed the evolution of TE materials through the complexity within the unit cell, nanostructuring, low dimensionality and defect controlling with wide range of frequency which would lead to high efficiency TE materials and fabrication of diverse TE devices. In recent years, wearable and flexible TE applications have been emerging as effective energy harvesting way. However, the power density of wearable and flexible TE applications are lower than that of the bulk, so we need to gather information on how to develop shapeless heat sources and new methods of TE device fabrication.

References

1. Rowe, D. M. Thermoelectric Handbook (CRC Press, 1995).
2. Snyder, G. J. & Toberer, E. S. Complex thermoelectric materials. *Nat. Mater*. **2008**, 7, 105–114.
3. M W. Thomson; On a mechanical theory of thermoelectric currents. *Proceeding softhe Royal Society of Edinburgh.* **1851**, 91.
4. Cutler, M., Leavy, J. F. & Fitzpatrick, R. L. Electronic transport in semimetallic cerium sulfide. Phys. Rev. 133, A1143–A1152 (1964).
5. Majumdar, Arun. Thermoelectricity in Semiconductor Nanostructures. *Science*. **2004**, 303, 777-778
6. Francombe M. H. Structure-cell data and expansion coefficients of bismuth telluride. *Br. J. Appl.* **1958**, 9, 415.
7. Goldsmid H. J.; Thermoelectric refrigeration. *Plenum press*. New York, **1964**.
8. Larson P., Mahanti S. D., and Kanatzidis M. G. Electronic structure and transport of Bi_2Te_3 and $BaBiTe_3$. *Physical Review B.* **2000**, 61, 8162.
9. Delavignette P. D. Dislocation Nets in Bi_2Te_3 and Sb_2Te_3. *Philos. Mag*. 5,**1960**, 729.
10. Miller G. R., Li C. Y., Spencer C. N. Properties of Bi_2Te_3-Bi_2Se_3 Alloys. *J. Appl. Phys.* **1963**, 34, 1398.
11. Horak J., Cermark K., Koudelka L. Energy formation of antisite defects in doped Sb_2Te_3 and Bi_2Te_3 crystal. *J. Pys. Chem. Solids.* **1986**, 47.
12. Horak J., Srary Z., Lostak P., Pancis J.. Anti-site defects in n-Bi_2Se_3 crystal. *J. Pys. Chem. Solids*. **1990**, 51, 1353.
13. Slack GA., CRC Handbook of Thermoelectrics, ed. DM Rowe, Boca Raton, FL: CRC Press (**1995**)
14. Sales B. C., Mandrus D., Williams R. K. Filled Skutterudite Antimonides: A New Class of Thermoelectric Materials. *Science.* **1996**, 272, 1325–1328.
15. Christensen M. Avoided crossing of rattler modes in thermoelectric materials. *Nat. Mater.* **2008**, 7, 811–815.
16. Di Xiao, Yugui Yao, Wanxiang Feng, Jun Wen, Wenguang Zhu, Xing-Qiu Chen, G. Malcolm Stocks, and Zhenyu Zhang. Half-Heusler Compounds as a New Class of Three-Dimensional Topological Insulators. *Phys. Rev. Lett*. **2010,** 105, 096404.
17. Poon S. J. Electronic and thermoelectric properties of Half-Heusler alloys. *Semicond. Semimetals.* **2001**, 70, 37.
18. Hicks L.D., Dresselhaus M. S. Effect of quantum-well structures on the thermoelectric Bgure of merit. *Physical Review B*. **1996**, 47, 19
19. Hicks L. D., Dresselhaus M. S. Thermoelectric figure of merit of a one-dimensional conductor.

Phys. Rev. B. **1993**, 47, 16631–16634.

20. Hicks L. D., Harman T. C., Sun, X., Dresselhaus M. S. Experimental study of the effect of quantum-well structures on the thermoelectric figure of merit. *Phys. Rev. B.* **1996**, 53, 16
21. Heremans J. P., Jovovic V., Toberer E. S., Saramat A., Kurosaki K., Charoenphakdee A., Yamanaka S. and Snyder G. J. Enhancement of Thermoelectric Efficiency in PbTe by Distortion of the Electronic Density of States. *Science*. **2008**, 321, 554–557.
22. B, Poudel. *et al*. High-Thermoelectric Performance of Nanostructured Bismuth Antimony Telluride Bulk Alloys. *Science.* **2008**, 320, 634–638.
23. Kim S. I., Lee K. H., Mun H. A, Kim H. S., Hwang S. W., Roh J. W., Yang D. J., Shin W. H., Li X. S., Lee Y. H., Snyder G. J., Kim S. W. Dense dislocation arrays embedded in grain boundaries for high-performance bulk thermoelectrics. *Science.* **2015**, 348, 109–114.
24. Yan X., Poudel B., Ma Y., W., Joshi G., Wang H, Lan Y., Wang D., Ren, Z. F. & Chen, G. Experimental Studies on Anisotropic Thermoelectric Properties and Structures of n-Type $Bi_2Te_{2.7}Se_{0.3}$. *Nano Lett.* **2010**, 10, 3373–3378
25. Hu L., Zhu T., Liu X, Zhao X. Point Defect Engineering of High-Performance Bismuth-Telluride-Based Thermoelectric Materials. *Adv. Funct. Mater.* **2014**, 24, 5211–5218
26. Liu W., Zhang Q., Lan Y, Chen S., Yan X., Zhang Q., Wang H., Wang D., Ren, Z. F. & Chen, G. Thermoelectric Property Studies on Cu-Doped n-type Cu_x Bi_2 $Te_{2.7}$ $Se_{0.3}$ Nanocomposites. *Adv. Energy Mater.* 2011, 1, 577–587
27. Hu L, Wu H, Zhu T, Fu C, He J, Ying P, Zhao X. Tuning Multiscale Microstructures to Enhance Thermoelectric Performance of n-Type Bismuth-Telluride Based Solid Solutions. *Adv. Energy Mater*. **2015**, 5, 1500411
28. Yazawa, K., Shakouri, A. Optimization of power and efficiency of thermoelectric devices with asymmetric thermal contacts *J. Appl. Phys.* **2012**, 111, 024509.
29. Bahk J. H., Fang H., Yazawaa K., Shakouria A. Flexible thermoelectric materials and device optimization for wearable energy harvesting. *J. Mater. Chem. C*, **2015**, 3, 10362
30. Varghese T., Hollar C., Richardson J., Kempf N., Han C., Gamarachchi P., Estrada D., Mehta R. J., Zhang Y. High-performance and flexible thermoelectric films by screen printing solution-processed nanoplate crystals. *Scientific Reports*. **2016**, 6, 33135.
31. Kim G-H., Shao L., Zhang K., Pipe K. P. Engineered doping of organic semiconductors forenhanced thermoelectric efficiency. *Nat mater.* **2013**, 12, 719-723
32. Kim S. J., We J. H., Cho B. J. A wearable thermoelectric generator fabricated on a glass fabric. *Energy Environ. Sci.* **2014**, 7, 1959-1965

Chapter 2. High performance thermoelectric painting

2.1 Sb_2Te_3-based chalcogenidometalate solution

Soluble Sb_2Te_3-based molecular chalcogenidometalate were synthesized by modifying the methodologies reported by Dmitri *et al*[1-4], who used N_2H_4 as solvents to dissolve bulk metal chalcogenides in the presence of elemental chalcogens. In the current study, instead of N_2H_4, thiol-diamine mixture was used as co-solvent to synthesize Sb_2Te_3 based chalcogenidometalate[5,6]. Typically, elemental Sb and Te powder with stoichiometric ratio of Sb_2Te_4 were dissolved in co-solvent of ethanethiol and ethylenediamine at room temperature, producing dark-purple solutions that held a high solubility (>100mg/mL) (Figure 2.1). Elemental analysis of Sb_2Te_3-ChaM using inductively coupled plasma optical emission spectrometry (ICP-OES) indicated overall ratio of Sb/Te of 2/1, identical to initial elemental ratio (Figure 2.2).

Fig. 2.1. Picture of Sb_2Te_3 based ChaM solution

Sample (Samp) **10/6/2015, 3:11:12 PM** **Tube 9**
Weight: 1 **Volume: 1** **Dilution: 25**

Label	Sol'n Conc.	Units	SD	%RSD	Int. (c/s)	Calc Conc.	DF
Sb 231.146	0.741	mg/L	0.015	2.0	961	18.5 mg/L	1.00
Te 238.579	1.48	mg/L	0.016	1.1	1155	37.0 mg/L	1.00

Fig. 2-2 ICP-OES result of dried Sb2Te3 based ChaM solution

2.1.1 XPS and XRD analysis of Sb_2Te_3-based chalcogenidometalate

In order to verify that successfully synthesized without the phase change or oxidization of Sb_2Te_3-based chalcogenidometalate, The X-ray photoelectron spectra analysis was conducted for dried Sb_2Te_4 clear solution. Figure 2.3 show that the peaks of Sb $3d^{3/2}$ and Sb $3d^{5/2}$ peaks correspond to Sb metallic bonding and the peaks of Te $3d^{3/2}$ and Te $3d^{5/2}$ peaks are Te homo-polar peak and Te metallic bonding.[7] These results indicate the formation of an ionic Sb_2Te_4 compound without phase change or oxidization

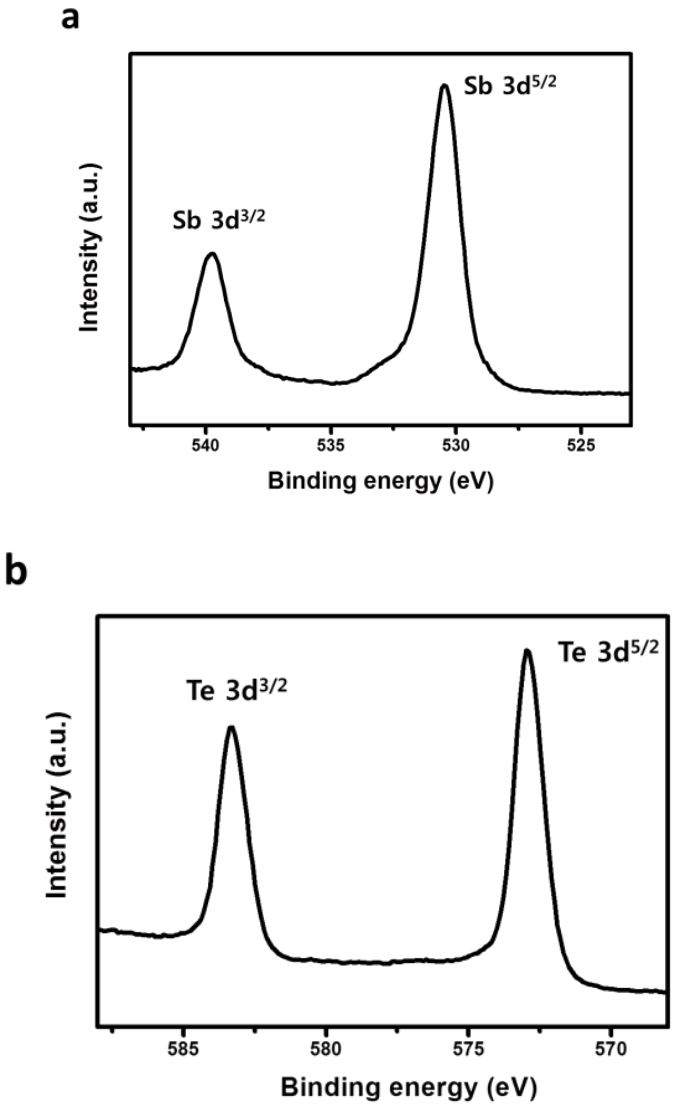

Fig. 2.3. XPS spectra of the Sb_2Te_3 ChaM dried at room temperature near (a) Sb region and (b) Te region.

Figure 2.4 present X-ray diffraction patterns of the Sb_2Te_3 ChaM. The result indicates that Sb_2Te_3 ChaM separate into two phase with formation of crystalline Sb_2Te_3 and Te phases during the heat treatment at 100 ^oC (red color), 200 ^oC (blue color), and 350 ^oC (green color). The peaks responding to Sb_2Te_3 and Te phases in the XRD pattern were more pronounced upon heating at more higher temperatures. The vertical dashed red and blue lines indicate the patterns of Te and Sb_2Te_3, respectively.

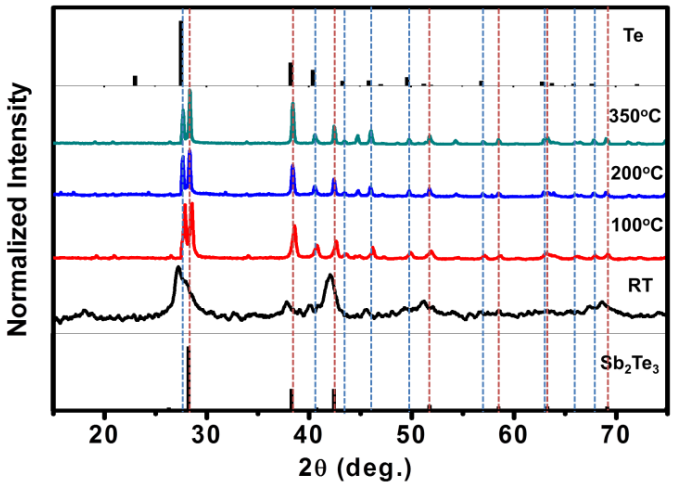

Fig. 2.4. XRD patterns for the Sb_2Te_3 ChaM annealed at various temperatures

2.1.2 DSC and TGA analysis of Sb2Te3-based chalcogenidometalate

Figure 2.5 shows the thermogravimetric (TGA) scan and Differential Scanning Calorimetry (DSC) of dried Sb_2Te_3-ChaM at room temperature. Dark cyan-coloured and navy-coloured lines indicate the heat flow and the weight loss respectively. The result presented that TGA scan of the dried Sb_2Te_3 ChaM sample at room temperature shows negligible weight loss until 450 °C which is consistent with previously reported Sb_2Te_3-based chalcogenidometalate[8]. The endothermal peak in DSC curve at about 420 °C corresponds to the melting point of a Te phase formed from the Sb_2Te_3 ChaM. It indicates the complete decomposition of Sb_2Te_3-ChaM into crystalline phases

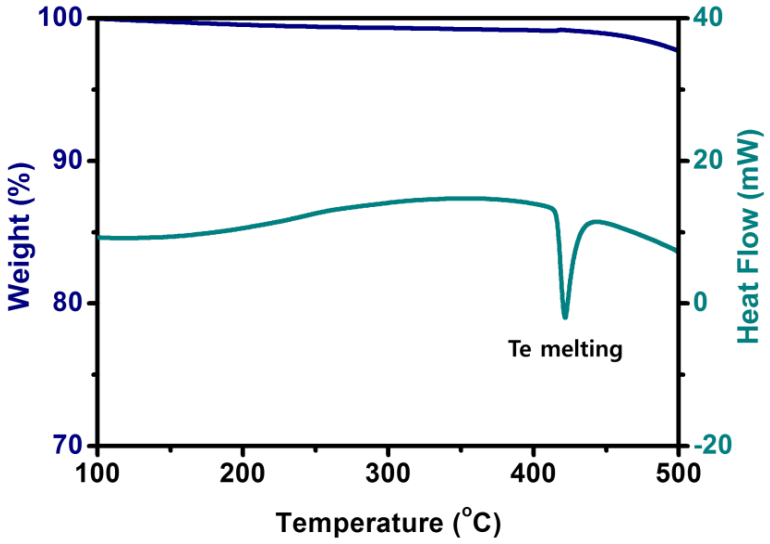

Fig. 2.5. TGA and DSC graph for the Sb_2Te_3 ChaM annealed at various temperatures

2.1.3 Applicability of Sb_2Te_3–based chalcogenidometalate solution in various solvents

Sb_2Te_3-ChaM was dispersible in various polar solvents with the dielectric constant (ε) ranging 10~50, including dimethyl sulfoxide (ε ≈ 47), dimethyl formamide (ε ≈ 36), and ethylenediamine (ε ≈ 13) and viscous polar solvents of ethylene glycol (ε ≈ 37) and glycerol (ε ≈ 43), which made it possible to adjust the properties of TE paints in terms of dielectric constant, solvent viscosity, and evaporation temperature.

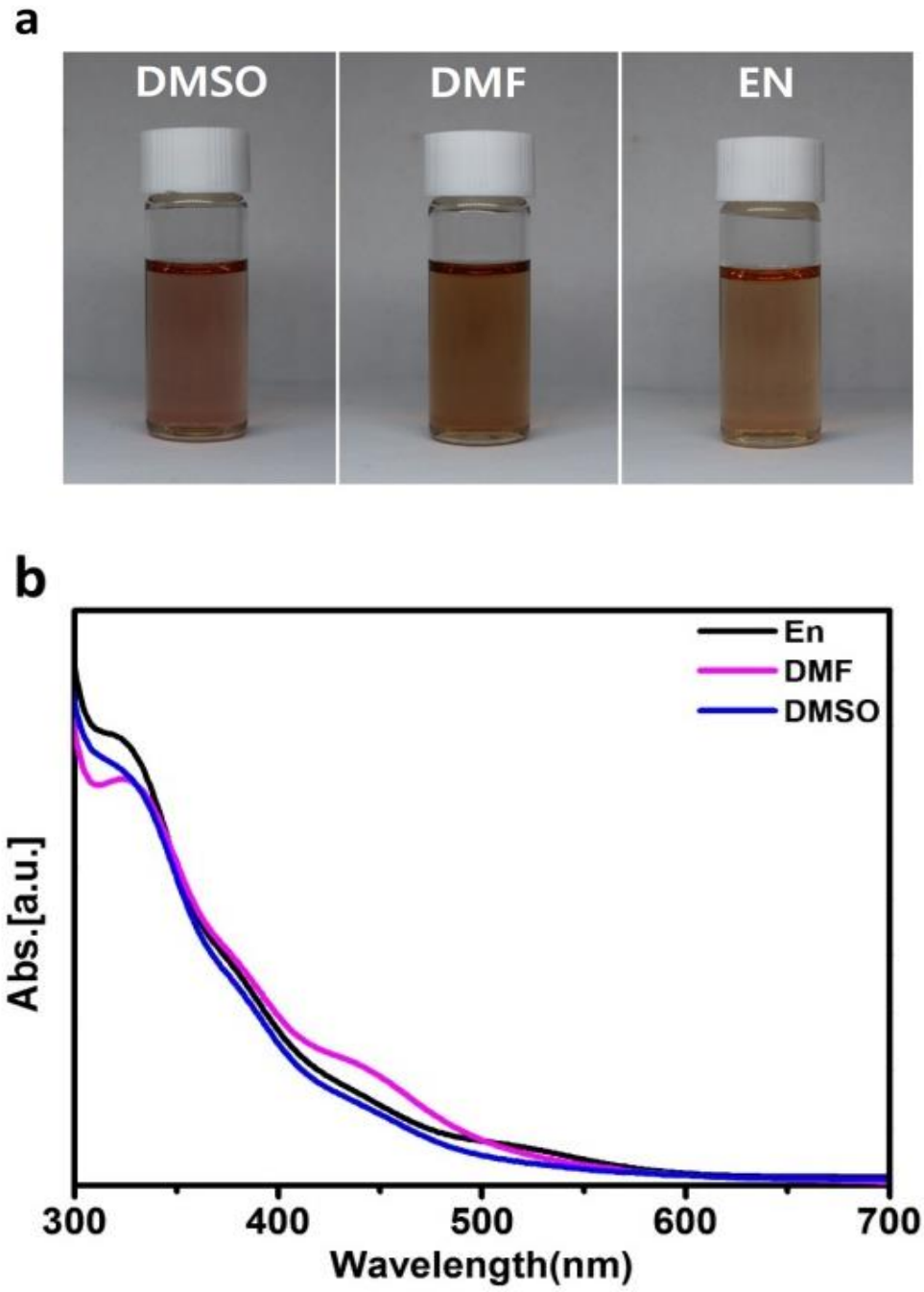

Fig. 2.6. (a) Photographs and (b) UV-visible absorption spectra of the Sb_2Te_3 ChaM dispersed in dimethyl sulfoxide (DMSO), dimethylformamide (DMF), and ethylene diamine (En) solvents.

2.2 Characterize of thermoelectric ink

In order to prepare TE paints, the powder with the chemical composition of $Bi_{2.0}Te_{2.7}Se_{0.3}$ (n-type) and $Bi_{0.4}Sb_{1.6}Te_{3.0}$ (p-type) were mechanical alloyed under nitrogen atmosphere using high energy ball milling. The Figure 2.7 indicated that the XRD patterns of $Bi_{2.0}Te_{2.7}Se_{0.3}$ and $Bi_{0.4}Sb_{1.6}Te_{3.0}$ TE powder. The XRD patterns of $Bi_2Te_{2.7}Se_{0.3}$ ball milled powder shift to the high angle in comparison with Bi_2Te_3 due to the addition of Se and $Bi_{0.4}Sb_{1.6}Te_{3.0}$ completely correspond to the bulk pattern[9,10].

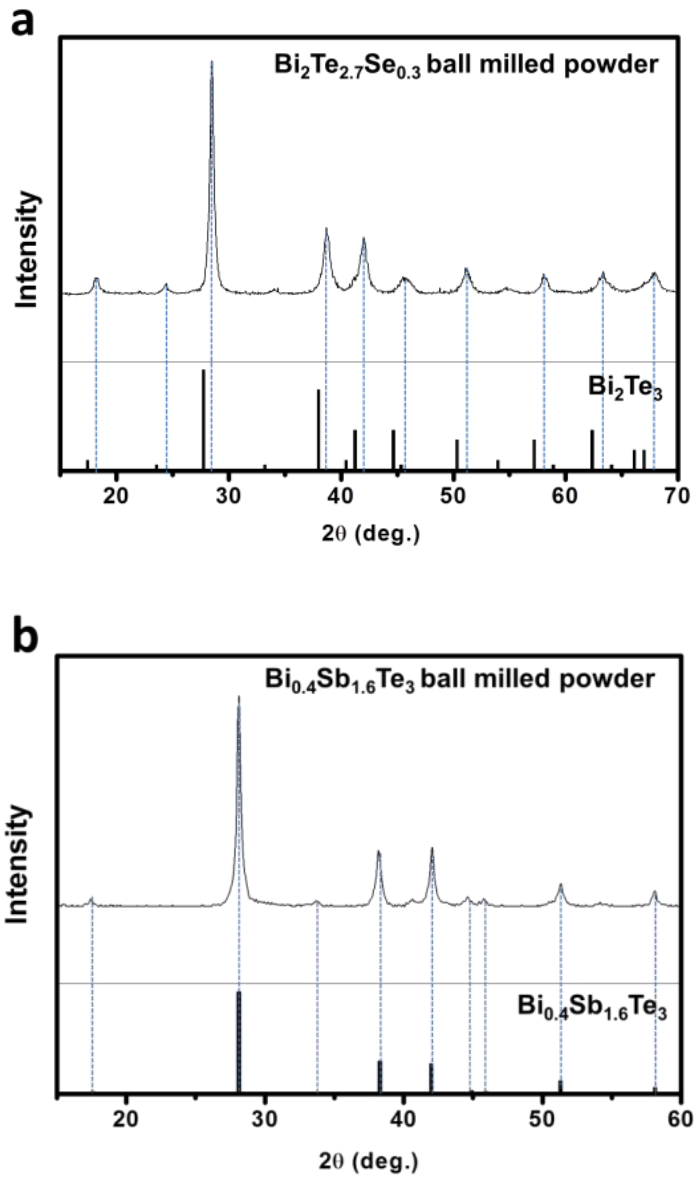

Fig. 2.7. XRD patterns of mechanical alloyed (a) $Bi_2Te_{2.7}Se_{0.3}$, (b) $Bi_{0.4}Sb_{1.6}Te_{3.0}$ TE powder.

We dispersed the Sb_2Te_3 ChaM with 20wt% of TE particles in a mixed viscous cosolvent of glycerol and ethylene glycol include of prepared n- and p-type TE microparticles. The viscosity and evaporation temperature of the TE paints were adjusted by controlling the ratio of glycerol (viscosity at room

temperature ≈ 934 mP•s, boiling point ≈ 290 °C) and ethylene glycol (viscosity at room temperature ≈ 62 mP•s, boiling point ≈ 197 °C). Stable TE suspensions were finally synthesized that have no phase separation and precipitation for more than a week. (Figure 2.8)

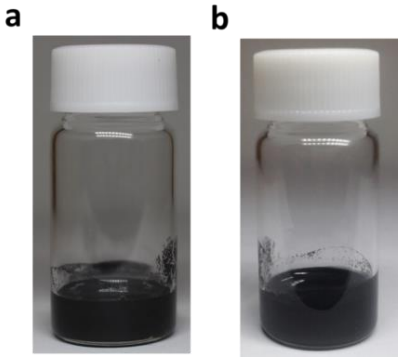

Fig. 2.8. Colloidal stability of the TE paint.

2.2.1 The effect of addition with the Sb_2Te_4 as a sintering aid

Painted and dried n- and p-type paints on aluminum plates were annealed at various elevated temperatures higher than 350 ºC, producing mechanically robust TE samples with several hundred micrometers in thickness. To determine the proper sintering temperature, DSC and TGA analysis were conducted about painted n- and p-type TE sample. The DSC result shown in figure 2.9 indicated that the first endothermal peak at about 420 ºC observed in both n-and p-type paints well agrees with the Te melting point and the next peaks at 590 ºC and 610 ºC correspond to melting point of a Bi_2Te_3 phase and a Sb_2Te_3 phase and TGA scan of TE paints showing no weight loss up to 450 ºC. The weight loss above 450 ºC due to the evaporation of liquid Te that those typically make Te vacancy defect which result in a slight degradation of properties defect[11]. Therefore, the optimum sintering temperature for the current study was taken at 450 ºC

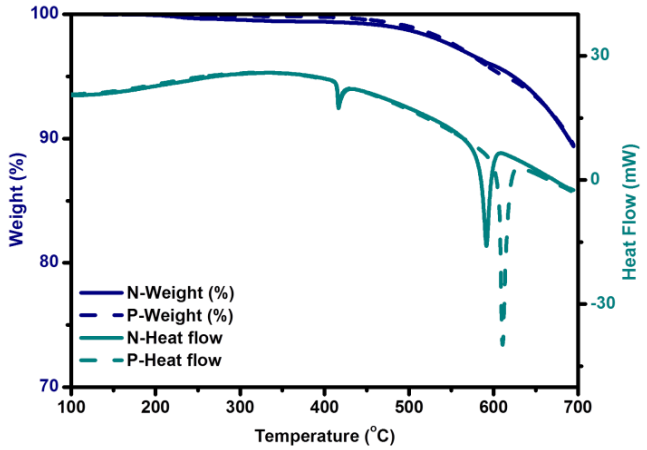

Fig. 2.9. DSC and TGA scans for the n-and p-type paints.

Upon heating, these TE paints showed effective sintering behaviors on both n-type $Bi_{2.0}Te_{2.7}Se_{0.3}$ and p-type $Bi_{0.4}Sb_{1.6}Te_{3.0}$ TE particles arising from the molecular Sb_2Te_3-ChaM effect. To explore the sintering behaviors of painted samples, the scanning electron microscopy (SEM) image of TE samples with and without the Sb_2Te_3 ChaM sintered at 450 °C are shown in Figure 2.10a and c. The SEM image of n- and p-type samples with ChaM shows huge densification effect which is attributable to an interconnecting effect of TE particles by ChaM. As control experiments, the suspension of TE particles without ChaM was painted and annealed under identical conditions. The resulting materials were mechanically weak upon annealing at even 500 °C. As shown in Figure 2.10b and 2d, TE particles were just partially sintered with numerous voids.

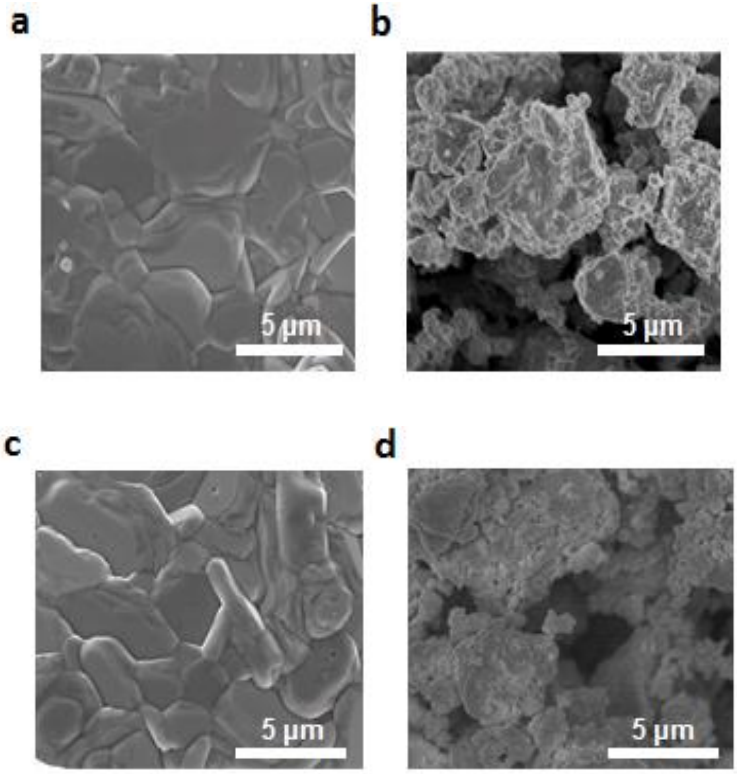

Fig. 2.10. SEM images of the annealed n-type materials (**a**) with and (**b**) without the ChaM, and the p-type materials (**c**) with and (**d**) without the ChaM.

The origin of microstructural characteristics of annealed TE paints should be related to Sb_2Te_3 ChaM placing between TE particles. The SEM images and elemental mapping images dried TE paints of ChaM obtained by the energy dispersive X-ray spectroscopy (EDS) indicated that molecular Sb_2Te_3-ChaM were homogeneously distributed into between TE particles without local agglomeration. (Figure 2.11)

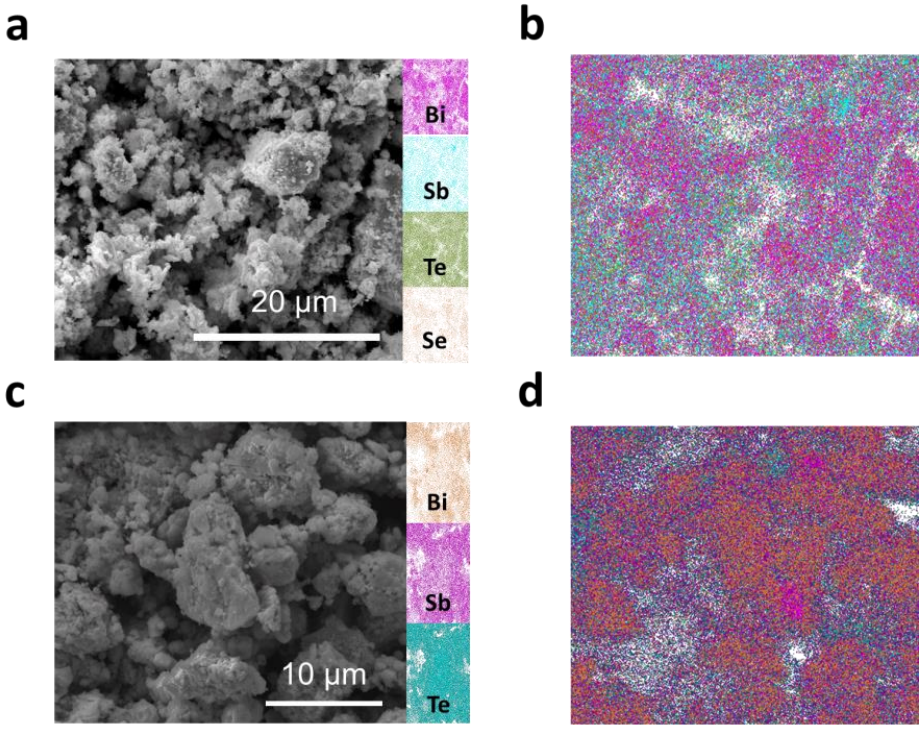

Fig. 2.11. SEM images of the dried samples of (a) n-type and (c) p-type and EDS mapping of (c) n-type and (d) p-type samples.

The densities of annealed paints with ChaM increased with annealing temperatures up to 3.9 g/cm^3 for n-type and 3.6 g/cm^3 for p-type. On the other hand, the densities of those samples without ChaM were less than 3.0 g/cm^3 and just 60~70% of materials prepared from TE paints with ChaM. (Figure 2.12) These results demonstrated effective densification and grain growth in all-inorganic TE paints due to Sb_2Te_3-ChaM effect.

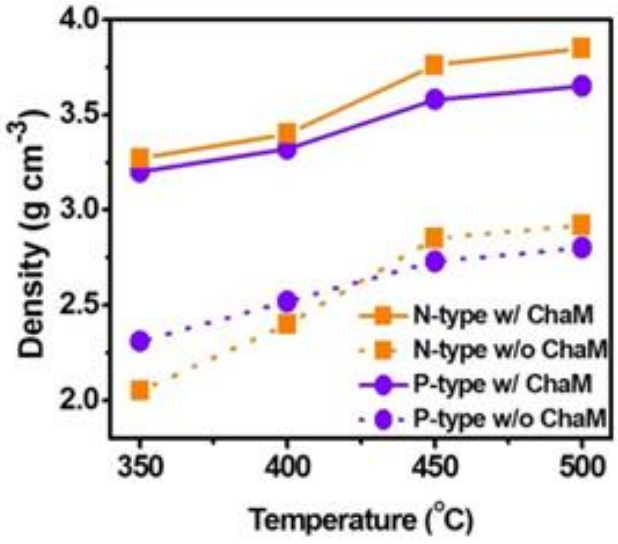

Fig. 2.12. Comparison of TE n- and p-type sample's density of with and without ChaM

Figure 2.13 shows microstructures of grain morphology indicates the grain growth in a layer-by-layer mode, which requires 2-dimensional nucleation event from a liquid medium as a prerequisite[12]. SEM image of the fractured surface dictates the stereotypical microstructure formed by a lateral growth and nucleation[12].(Figure. 2.13) This further suggests that the sintering aid formed a liquid phase at the sintering temperature, providing a diffusion path for grain growth. The DSC curves of n-and p-type paints (Figure 2.9)indicated that the Te phase formed from the Sb_2Te_3 ChaM sintering aid is melted at ~420 ^oC. This evidence show that liquid phase sintering result from liquid form of Te.

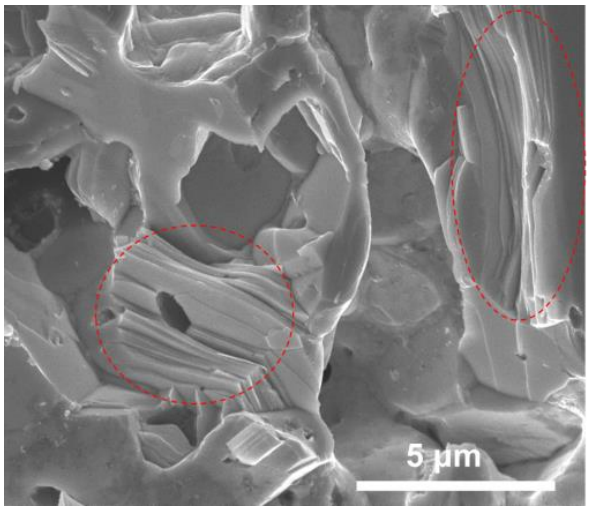

Fig. 2.13. SEM image of the fractured surface of annealed sample

Based on the analysis on a time dependent shrinkage measurement as shown in figure 2.14, where the time exponent of 0.08 is much smaller than the theoretical value, Other factors from the viscous flow mechanism during the initial stage of the liquid phase sintering was exclude. The viscous flow mechanism during liquid-phase sintering is represented as the following relation[13]: $\Delta l/l \propto t^{1+y}$, where l is a linear dimension of the sample and t is sintering time. Because of enhanced driving force with reducing pore volume during the sintering process, the exponent 1+y is a little than unity.

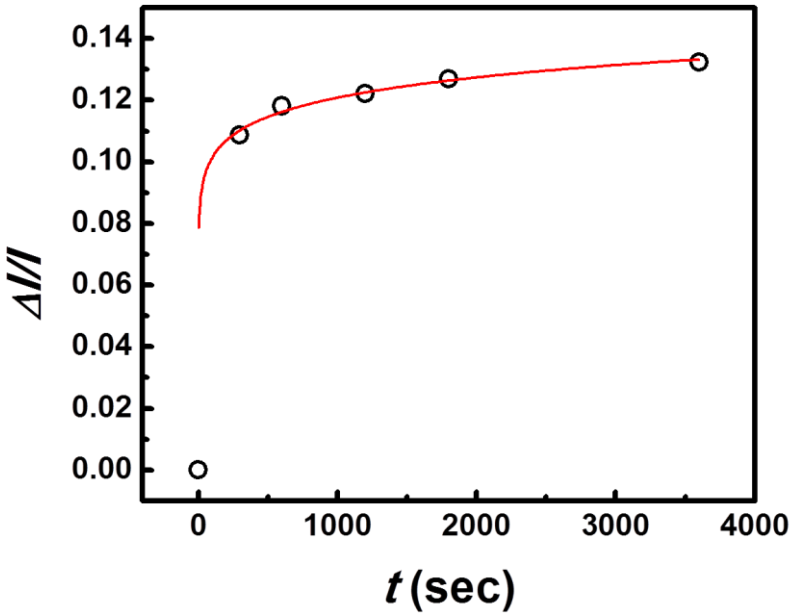

Fig. 2.14. A shrinkage vs. time plot of the n-type paint during sintering at 450 °C

The temperature-dependent XRD patterns (Figure 2.15) manifested that the Sb_2Te_3 ChaM was completely consolidate into the host phase due to compositionally well harmony with host phases. It is more prominented in n-type materials. Figure 2.16 shows the existance of peak shift to lower angle with increasing the sintering temperature. It means the increase of Te stoichiometric ratio in a BiSbTe phase due to the combination between the Sb_2Te_3 ChaM with the host phase.

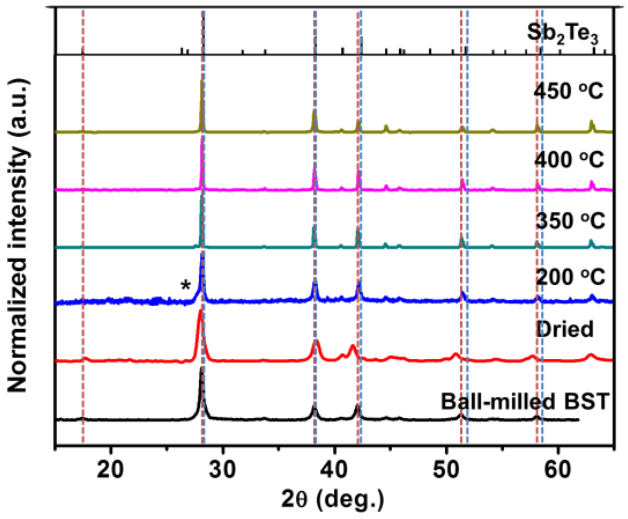

Fig. 2.15. XRD patterns of n-type $Bi_{0.4}Sb_{1.6}Te_3$-Sb_2Te_3 ChaM paint

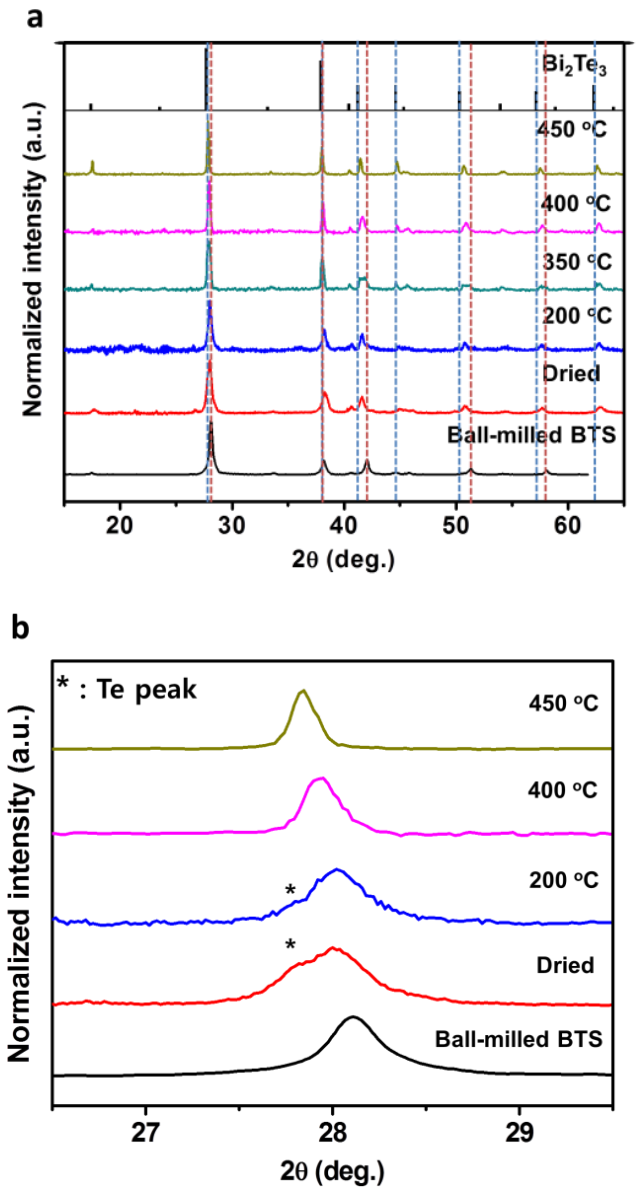

Fig. 2.16. XRD patterns of n-type $Bi_2Te_{2.7}Se_3$-Sb_2Te_3 ChaM paints. (a) XRD patterns of the n-type samples as a function of sintering temperatures. (b) Enlarged XRD patterns at the range from 26° to 31°

Improved sintering properties of TE paints with ChaM critically influenced the electrical charge transport. The electrical conductivity of n- and p-type materials prepared from TE paints with ChaM increased up to 650–750 S cm^{-1} at room temperature, which were one order of magnitude higher than the molded samples from TE suspension without ChaM. (Figure 2.17)

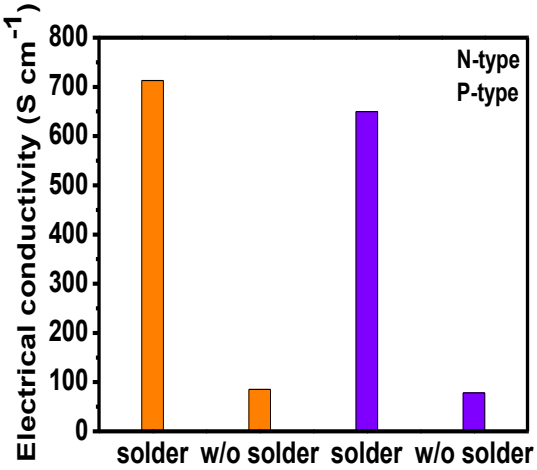

Fig. 2.17. Comparison of TE n- and p-type sample's Electrical conductivity of with and without ChaM

2.2.2 Thermoelectric properties of n- and p-type sintered sample

Dense and well-sintered grains in painted TE samples resulted in excellent TE properties in both n- and p-type samples. TE properties of painted n- and p-type samples annealed at 450 °C were characterized at measuring temperatures ranging from 25 °C to 125 °C.

The temperature dependence of electrical conductivities of n-and p-type samples in Figure 2.18. The electrical conductivity of the n-and p-type samples gradually decreased as the ambient temperature increased to 125 °C, which indicates a metallic conducting behavior. The maximum electrical conductivity of the n-and p-type samples 650–750 S cm^{-1} at room temperature which were similar with the properties of hot-pressed or spark plasma sintered Bi_2Te_3 based TE materials with 700~1100 S cm^{-1}. These high electrical conductivities arise from the appropriately high carrier mobility of 149 cm^2 V^{-1} s^{-1} for the n-type and 141 cm^2 V^{-1} s^{-1} for the p-type materials.

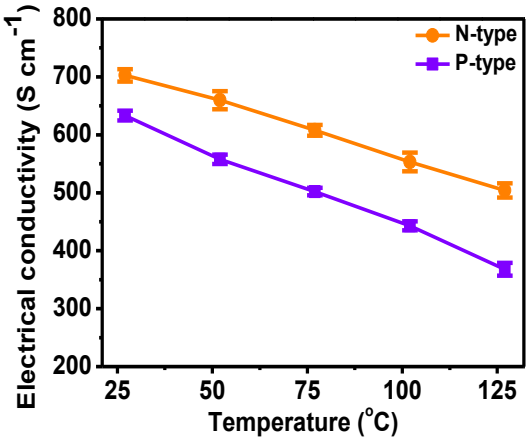

Fig. 2.18. Temperature dependence of electrical conductivity for TE n- and p-type samples

The temperature dependence of electrical conductivities of n-and p-type samples in Figure 2.19. The absolute seebeck coefficient value of TE n- and p-type samples were increased as the temperature increased at 100 °C and then began to decrease. This behavior is characteristic feature of a highly degenerate semiconductor due to the reduction of carrier concentration result from the Fermi level is moving up to valence band maximum with temperature increased. The Seebeck coefficient of n- and p-type samples were 115 μV/K and 170μV/K at room temperature and the peak value reached 135 μV/K and 190 μV/K at 375 K, respectively. The high carrier concentrations of 3.0 x 10^{19} cm^{-3} for n-type samples and 2.9 x 10^{19} cm^{-3} for p-type samples[14,15] result in those relative low Seebeck coefficients. As well, It was founded that the annealing temperature affected the electrical properties of n-and p-type painted samples. The figure 2.20 shows SEM images of n- and p-type painted samples with increasing annealing temperatures that could be attributed to the increased grain sizes and densities arising from Sb_2Te_3-ChaM effect to interconnect grains with the annealing temperatures.

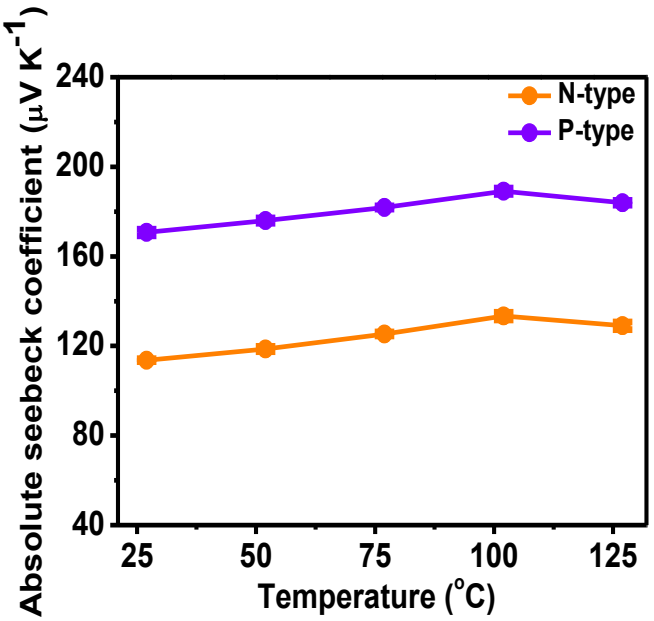

Fig. 2.19. Temperature dependence of absolute Seebeck coefficient for TE n- and p-type samples

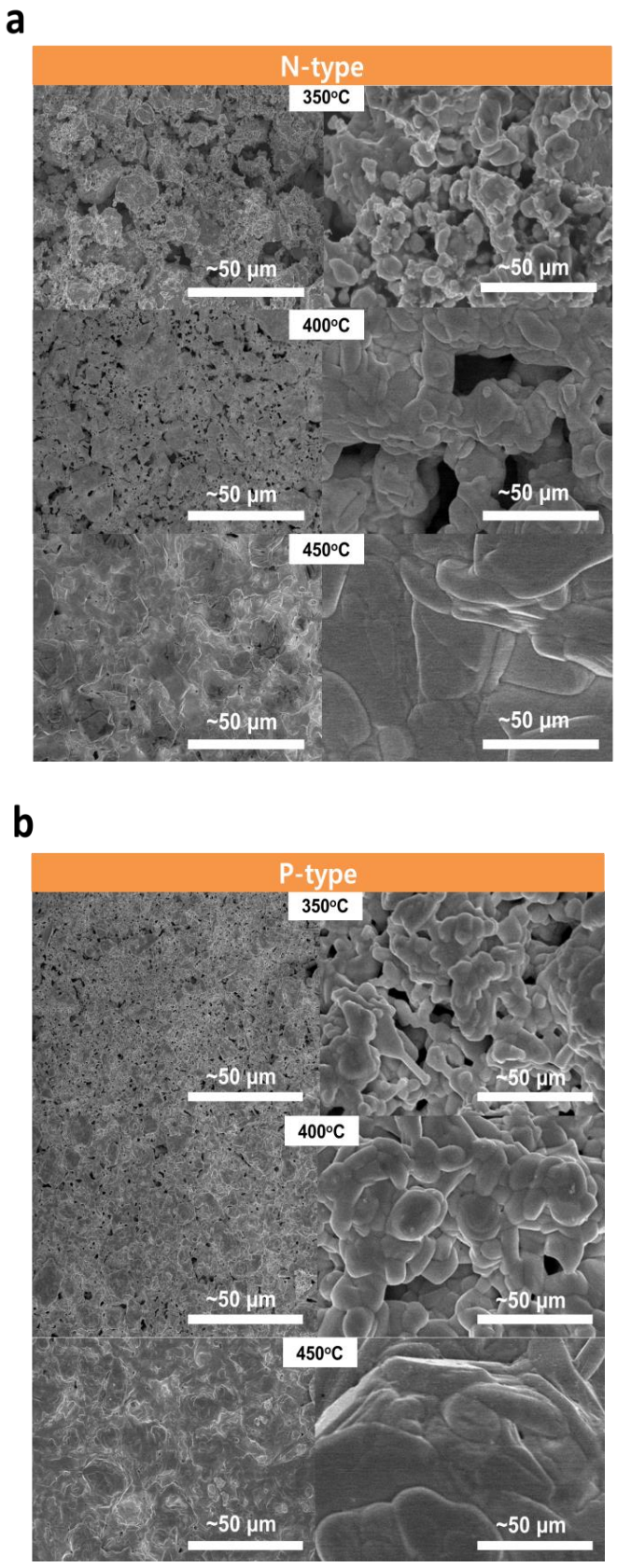

Fig. 2.20. SEM images of n-type (a) and p-type (p) TE paints sintered at various temperatures.

The most significant effect of molecular ChaM-assisted sintering is seen in the great reduction in the thermal conductivities of the n- and p-type samples (Figure 2.21), *i.e.*, 0.5–0.6 W m^{-1} K^{-1} in comparison with the 1.5–2.5 W m^{-1} K^{-1} of bulk Bi_2Te_3-based materials[16].

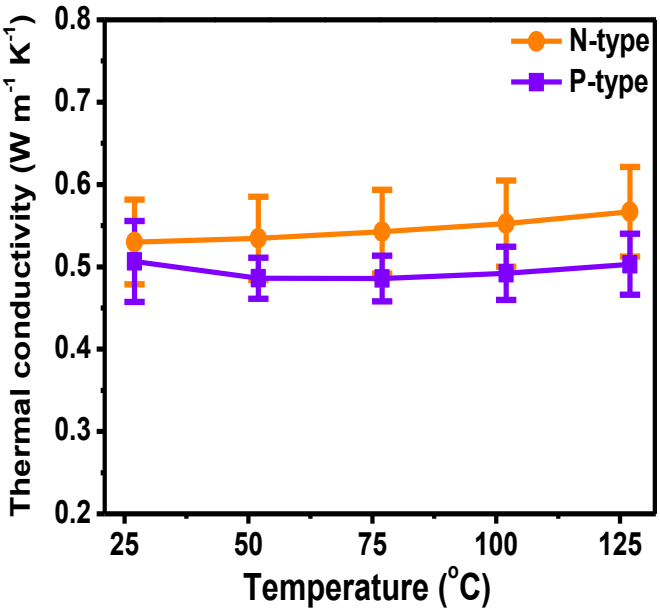

Fig. 2.21 Temperature dependence of thermal conductivity for TE n- and p-type samples

The thermal conductivity is the sum of electronic and phonon contribution, which is called the lattice thermal conductivity (κ_l). The lattice thermal conductivity can be calculated by subtracting the electronic contribution to the thermal conductivity (κ_e) from total thermal conductivity (κ), which was estimated by using the Wiedemann-Franz Law ($\kappa_e = LT\sigma$, where T is the absolute temperature, L is the Lorenz number, σ is the electrical conductivity). The Lorenz number of 2.0×10^{-8} V^2 K^{-2} is the typically used value for a degenerate semiconductor. However, in the recently published papers, the more reliable calculated value of ~1.6×10^{-8} V^2 K^{-2} was widely used in Bi_2Te_3 related materials. Based on this value, the minimum calculated κ_l was 0.19 W m^{-1} K^{-1} for n-type and 0.20 W m^{-1} K^{-1} for p-type painted materials. These values are lower or comparable than the predicted minimum κ_l of 0.31 W m^{-1} K^{-1} in n-type Bi_2Te_3 and 0.20 W m^{-1} K^{-1} and p-type $(Bi,Sb)_2Te_3$. It using the Debye-Callaway model[17], whereas the densities of painted materials are at most 50~55% of full densities. (Figure 2.22)

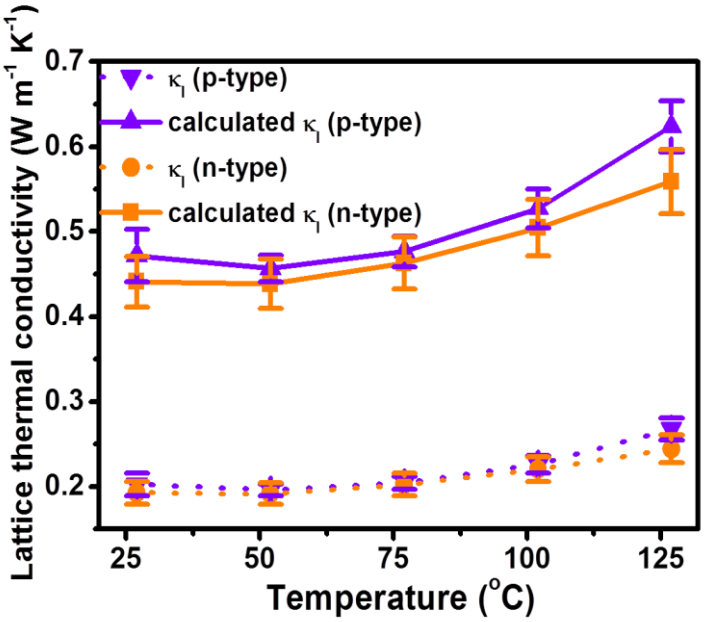

Fig. 2.22. Temperature dependence of calculated lattice thermal conductivities of n- and p-type painted samples using the modified formulation of the effective medium theory

The improvement of *ZT* values in nanostructured TE materials originates in the falloff of thermal conductivity by phonon-grain boundary scattering arising from the increased interface density. The grain sizes of the painted samples range from several hundred nanometres to several micrometres so that their ultralow lattice thermal conductivities are difficult to be explained solely by grain boundary scattering.

One possible explanation for the ultralow lattice thermal conductivity is the porosity of materials because the porosity in the painted samples reach 45~50%, which suggest that the phonon scattering at multiple pore sites can be a crucial factor to the reduced thermal conductivity.

The Brunauer Emmett and Teller (BET) measurement was conducted to analyse the porosity(Figure 2.23). Both n-and p-type samples have pores with the size less than 50 nm, which should be located at the interfaces formed from Sb_2Te_4 sintering aids rather than grains insides. These small pores can act as scattering sites for phonons with short wavelengths. However, the volumes of these small pores are responsible for only 2~3% porosity in the painted samples, calculated based on the measured pore volumes, which suggests the existence of micro-scale pores.

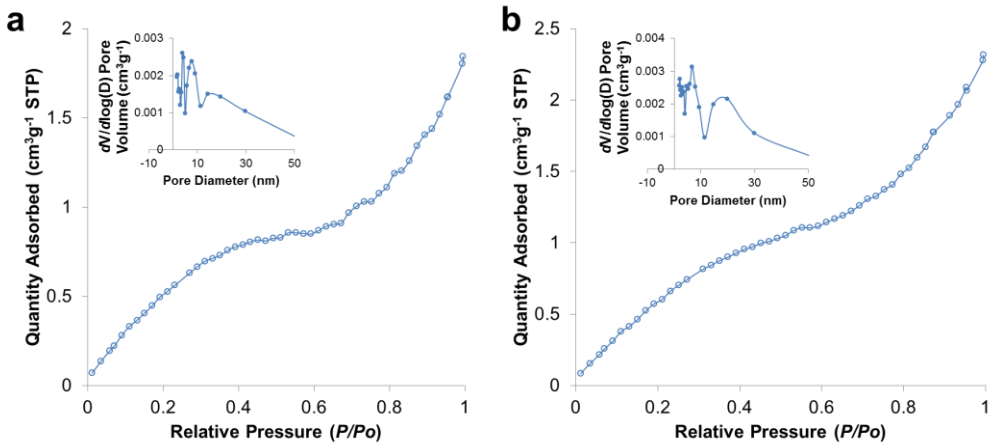

Fig. 2.23. Nitrogen adsorption-desorption isotherms of the painted (a) n-and (b) p-type samples. The inset shows the pore size distributions.

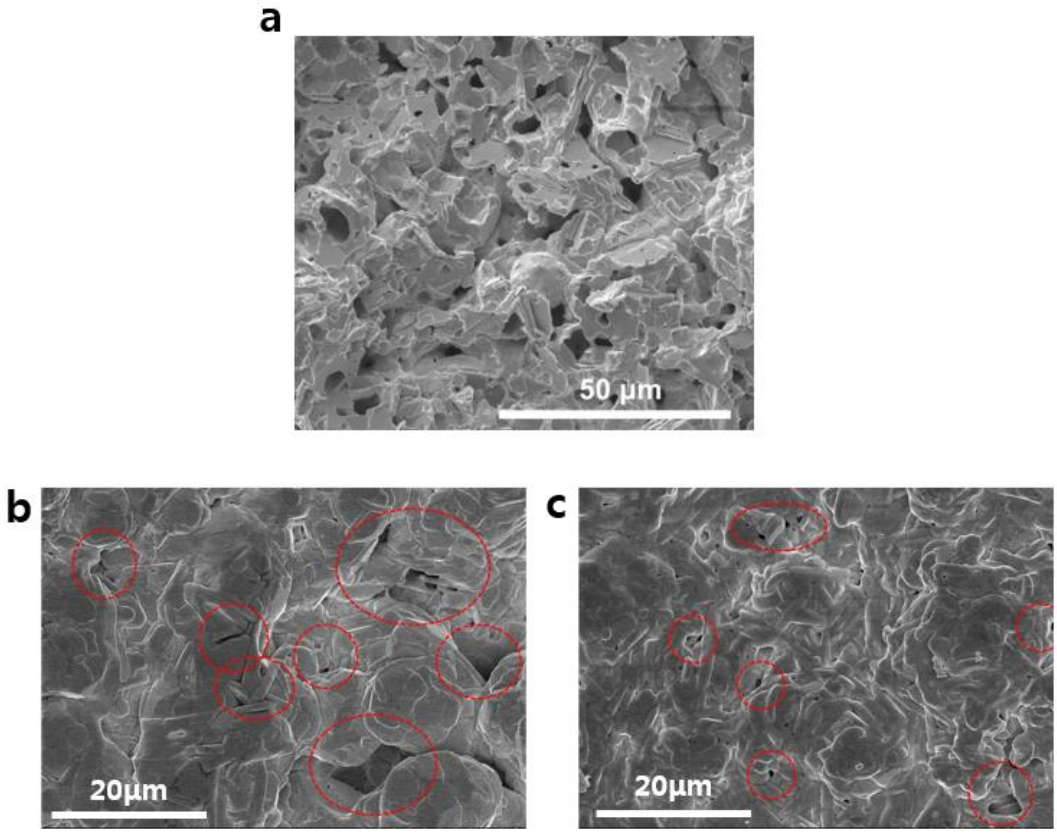

Figure 2.24. Low-magnification SEM images of fractured structure (a) and surface of painted sample. (b) n-type, (c) p-type. The red circles show the micro-scale pores in the samples.

To confirm the micro-scale pores, the microstructure of the painted samples was analysed by the SEM. As shown in Figure 2.24, the multiple pores with the size ranging from several tens of nanometres to several microns were clearly observed in the SEM images. Given that the presence of multi-scale pores can reduce the thermal conductivity by phonon scattering with a broad range of wavelength at pore sites,

the ultralow thermal conductivities of painted TE materials can be explained by the porosity.

To quantitatively estimate the porosity effect on the thermal transport, The thermal conductivity was compute the using the effective medium theory proposed by Lee et al.[18] $\kappa_l = \kappa_h((2-2\Phi))/((2+\Phi))$, where κ_h and Φ is the lattice thermal conductivity of host materials and the porosity respectively. The calculated minimum κ_l of the n-and p-type painted samples are 0.44 W m^{-1} K^{-1} and 0.47 W m^{-1} K^{-1} (Figure 2.22) respectively, which are comparable to those of typical nanostructured bulk materials prepared from ball-milled Bi_2Te_3-based TE materials. Consequently, these results suggest that the porosity of painted samples can be a crucial factor to the reduced latticed thermal conductivity for boundary scattering of phonons at pore sites, rather than grain boundaries.

Generally, the porosity of solid materials strongly affects the charge carrier transport due to scattering of carriers at the pore sites.[19] A charge carrier passing near a pore is scattered due to the potential perturbation[18], degrading the carrier mobility and eventually the electrical conductivity. The carrier scattering effect on mobility can be qualitatively described by the Matthiessen's rule[18]

$$\frac{1}{\mu_{\text{tot}}} = \frac{1}{\mu_{\text{bulk}}} + \frac{1}{\mu_{\text{impurity}}} + \frac{1}{\mu_{\text{boundary}}} + \frac{1}{\mu_{\text{pore}}} \quad (1)$$

Accordingly, the total scattering is the sum of the contribution of different carrier scattering mechanism. For example, μ_{bulk} is the mobility induced solely by the carrier scattering with acoustic phonons. In the painted materials, considering no additional impurity element except Bi, Sb and Te, μ_{boundary} and μ_{pore} should be the critical factors to determine the overall mobility. Lee *et al.* suggested that the porosity effect on electrical properties become weaker for larger grains[18]. Since the material with larger grains necessarily has larger pores with the lower number density under the same porosity, the scattering rate is reduced and mobility is enhanced for larger grain sizes. The fact that the grain size is in the range of several micrometres and the pores are mainly macro-scale in the painted materials (less than 3% of micro-pores in volume) suggests that the moderately high mobility is attributed to the lower number density of the pore.

The efficiency of the TE material is represented by the dimensionless figure of merit(*ZT*) and ZT=1 correspond to about 10% of total energy conversion efficiency. To reach the high value of *ZT*, It needs to have high Seebeck coefficient, high electrical conductivity and low thermal conductivity. The *ZT* value was calculated using the thermal conductivity, electrical conductivity and thermal conductivity. Figure 2.25 shows the temperature dependence of *ZT* for the n- and p-type sample. The highest values of $ZT = 0.68$ for n-type at 375 K and 1.15 for p-type at 350 K were achieved. It is noteworthy that those values were much higher than those of Bi_2Te_3 based bulk ingots with single crystal or Polycrystalline of $ZT \approx 0.8–1.0$[16] and comparable to those of recent nanostructured TE materials with $ZT \approx 1.1–1.7$[20-23]. Especially, as far as we know, these exceedingly high *ZT* values in current painted materials are 3–4

times higher than the best reported values of screen-printed TE pastes[24]. The high electrical conductivities and ultra-low thermal conductivities led to remarkably high TE *ZT* values of n-and p-type painted samples.

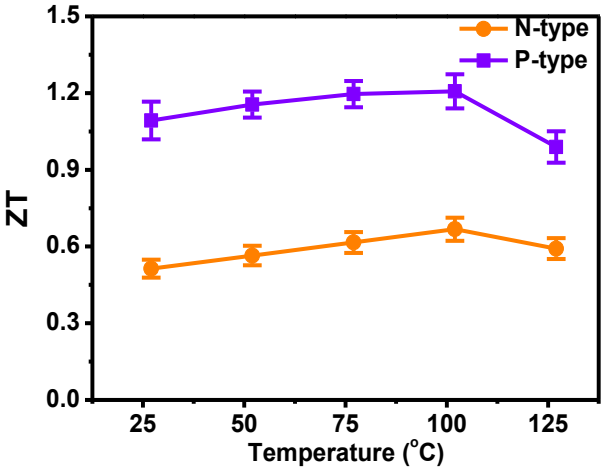

Fig. 2.25. Temperature dependence of *ZT* for TE n- and p-type samples

2.3 Fabrication of in-plane type thermoelectric devices via painting process.

2.3.1 The process of thermoelectric painting

The synthesized n-and p-type TE paints were painted on glass, aluminum, polyimide, and alumina substrates with a flat painting brush. Painted layers on a substrate were sequentially dried on a hot-plates at 90 ºC for 30 min ~ 60 min, 120 ºC for 30 min ~ 60 min, and 150 ºC for 30 min ~ 60 min and then they were annealed at desired temperatures with 350~450 ºC for 10~30 min. To obtain thick painted layers with several hundreds of micrometers in thickness, painting and drying processes were repeated by several times, followed by annealing. In-plane type TE devices were fabricated by painting five couples of Sb_2Te_3-ChaM assisted n-and p-type TE paints with the size of 5 mm x 10 mm on various substrates such as flat glass and polyimide, and curved hemi-cylindrical convex and concave glasses, and alumina hemi-sphere. Glass and alumina substrates were hydrophilized by a UV plasma treatment for 1 h before painting. Silver paste was painted electrically in series and thermally in parallel in order to interconnect n-and p-type TE legs. Nitrogen-filled glovebox is used for all experiment.

2.3.2 Output characteristics of in-plane thermoelectric devices on flat substrates

In the first case of all-painted TE devices, n-and p-type TE paints were painted on a flexible polyimide substrate with a brush and painted layers were dried. Surprisingly, the painted layers formed continuously uniform films with the thickness of ~50μm during annealing. It seemed to smooth out the uneven surfaces composed of TE particles via filling up void spaces with molecular Sb_2Te_3-ChaM.

Metal electrodes were also prepared by painting of Ag paste on pre-painted and annealed TE layers. This all-painted TE device was comprised of 5 couples of n-and p-type legs with the lateral dimension of 5 mm × 10 mm and the average thickness of ~50μm. (Figure 2.26)

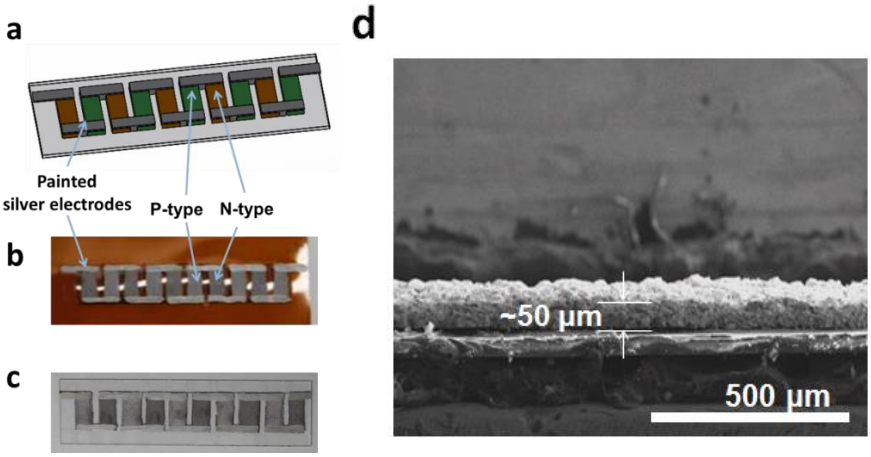

Fig. 2.26. (a) Scheme and photographs of an in-plane type TE devices composed of painted legs with silver electrodes on a (b) polyimide substrate and (c) glass substrate. (d) Cross-sectional SEM image of painted TE device

In manufacturing the TE device, TE materials well attached to the electrode is highly important factor for determine the power of device. The internal resistance of this device was 25.8 Ω, higher than the expected resistance in relation with the electrical properties. It might be due to the high contact resistance between the Ag electrode and the TE leg. In order to investigate the cause for high resistance of the TE device, The contact resistance between the Ag electrode and the painted TE leg was measured by the transmission line method. The measured contact resistance is quite high at 4.8×10^{-2} Ω cm^2.(Figure 2.27) That value is three or four orders of magnitude higher than the contact resistance observed in conventional module composed of Bi_2Te_3-based TE legs[25].

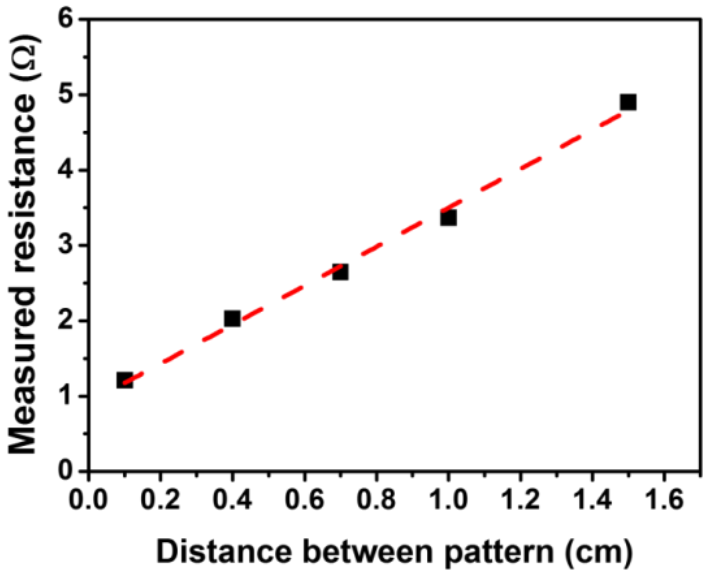

Fig. 2.27. Contact resistance measurement by the transmission line method

The output voltage of all-painted TE device on a polyimide substrate exhibited voltage of 79.4 mV and output power of 60.8 μW at temperature difference of 50 ºC. (Figure 2.28a) The output power density reached 2.43 mW/cm^2 (Figure 2.28b), which considerably exceeded the best reported values of in-plane typed TE devices by ~2 times. Also, 60 μW-level output power offer the potential for wearable TE devices for harvesting energy from human body as an auxiliary power supply. All-painted TE devices on a hydrophilized glass substrate were prepared under same preparation conditions. The internal resistance, output voltage, out power and density (Figure 2.28c and d) were ~20 Ω, 79 mV, 59 μW, and 2.4 mW/cm^2 respectively, which were almost identical to those of all-painted TE devices on a polyimide substrate, suggesting the consistency of TE painting process on various substrates.

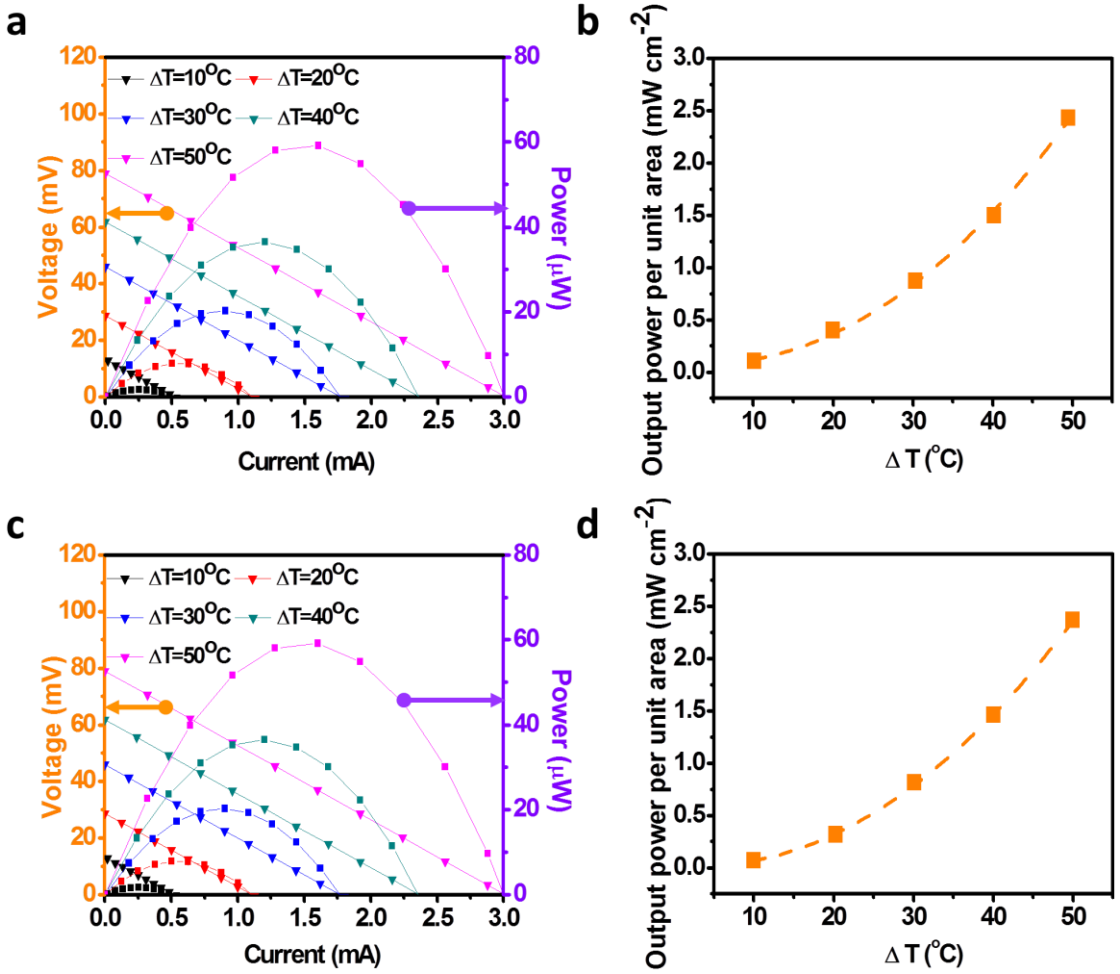

Fig. 2.28. Output characteristics of in-plane TE devices painted on flat substrates.

Output characteristics of in-plane TE devices painted on plate substrates. (a,b) Output power and power density of a polyimide substrate TE device (c,d) Output power and power density of a glass substrate TE

2.3.3 Output characteristics of in-plane thermoelectric devices on curved substrates

Such versatility of TE paints allowed us to apply TE layers on curved surfaces to directly prepare TE devices on curved heat sources. As shown in Figure 2.29, TE paints were painted on concave and convex surfaces of hydrophilized glass hemi-cylinder and were annealed at 450 °C, followed by painting of Ag pastes to interconnect n- and p-type layers. The resulting all-painted TE devices on curved surfaces were composed of 5 couples of n- and p-type layers with the lateral dimension of 5 mm × 10 mm and the expected thickness of ~50 μm (Figure 2.29a and 2.29b). Internal resistances of TE devices on convex and concave surfaces were identical values of ~20 Ω, which was consistent with those of the painted TE devices on flat substrates. Under temperature difference of 30 °C, these devices produced the output voltage of 31~35 mV and output power of 17~18 μW, respectively, leading to comparable values of 0.7

mW/cm^2 to those of the painted TE devices on flat glass substrates under same temperature difference (Figure 2.29c and 2.29d for a concave device, and 2.29e and 2.29f for a convex device). Especially, output power densites of all TE devices painted on flat and curved substrates with same dimensions of TE layers reached into the same line, which demonstrated the applicability of TE paints on any-shaped surfaces.

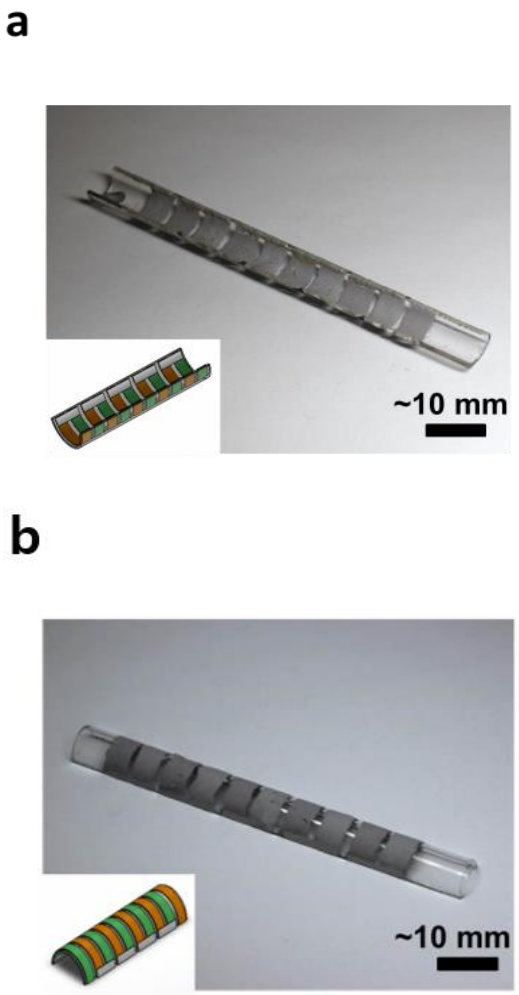

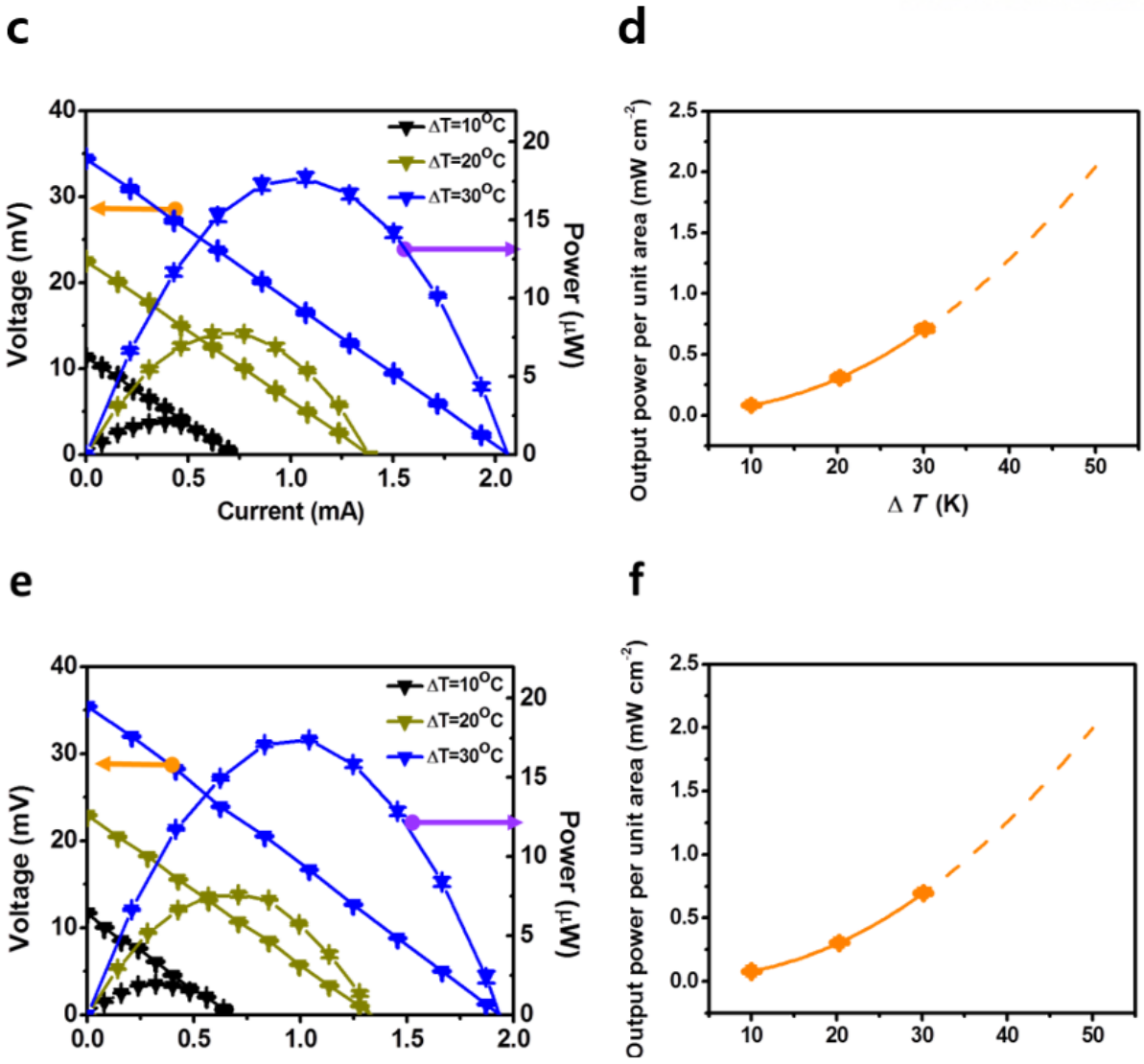

Fig. 2.29. Output characteristics of in-plane TE devices painted on curved substrates. (a) Photo of a concave device, (b) Photo of a convex device (c,d) Output power and power density of a concave device (e,f) Output power and power density of a convex device

2.4 Fabrication of hemispherical thermoelectric device via Painting process

New-typed all-painted TE devices were prepared comprising 5.5 couples of triangle-shaped TE layers with ~20 mm in base and 25 mm in height on large-sized ceramic hemi-sphere (diameter~50 mm) which collected heat energy from a bottom side. Internal resistance of this TE device was ~32 Ω, higher than those of other devices due to large-sized TE layers with 25% higher aspect ratio.

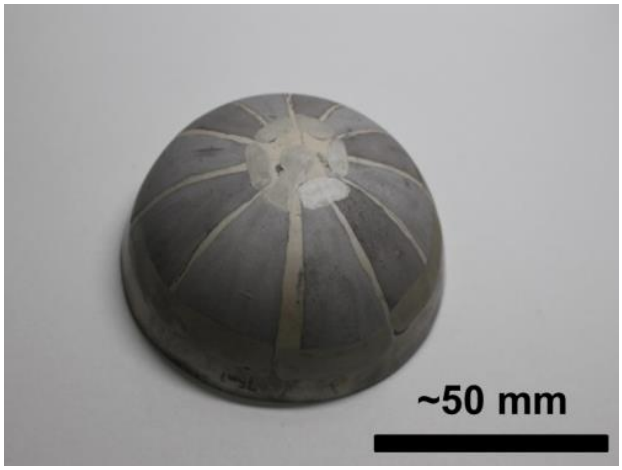

Fig. 2.30. Photo of hemispherical TE device via Painting process

2.4.1 Simulation study on the power output.

The comparative simulation study was investigated on the power output of the painted TE generator and the conventional module on a curved heat source using COMSOL. The model calculates the temperature distribution and generated power of the TE generators integrated with a heated hemispherical alumina substrate. The TE generator composed of one pair of n-and p-types of TE layers and conductive paste layers where the thickness was assumed as 50 μm. Each triangular TE layer has a width of 20 mm and a height of 60 mm such that the substrate has sufficient area for 5.5 couples of TE layers. The conductive paste was assumed to have the thermal conductivity of 9 W $m^{-1}\cdot K^{-1}$ and the electrical conductivity of 103 S cm^{-1}. Based on the geometry and the material properties, the electrical resistance was estimated as 3.5 Ω per a pair of the TE layers. Based on the survey of the material properties and the geometry for commercial TE modules, It was defined that a standard TE module has a substrate area of 40 mm × 40 mm and ~100 pairs of Bi-Te materials. The considered module has the thermal conductance of 0.65 W K^{-1}, the electrical resistance of 2.3 Ω, and the Seebeck coefficient of 52.8 mV/K. For the simple modeling, the FEM for the conventional module includes only one leg of TE material. The heat loss in the FEM was considered by including the convective heat transfer. To simulate the natural convection over all the surfaces that are exposed to air, the convection heat transfer coefficient was 10 W m^{-2} K^{-1} with an ambient temperature of 25 ^{o}C. [ref. 26]

The temperature distribution of the conventional module is greatly non-uniform (Figure 2.31) since the contact area (*d*) with a hemisphere is narrow which results in a significantly low output voltage of 13.3 mV for d = 1 mm and 4.5 mV for d = 0.1 mm. Thus, conventional module generates the output power of 76.9 μW and the output power density of 15 μW cm^{-2} when d = 1mm. when d = 0.1mm, the output power of 8.6 μW and the output power density of 1.7 μW cm^{-2} which are considerably reduced values compared with the reported values of 4-10 mW cm^{-2} obtained on a flat heat source[27].

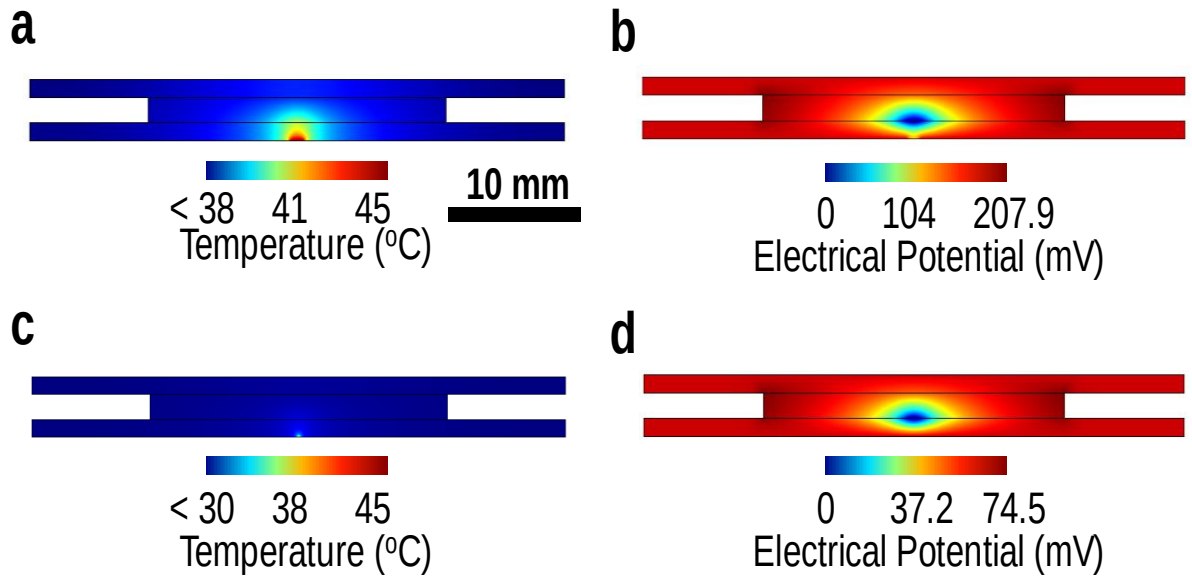

Fig. 2.31. Calculated (a,c) temperature and (b,d) electrical potential distribution of a conventional TE module that is contact on a heated hemispherical substrate.

On the other hand, the temperatures distribution of a hemispherical type module was kept at 45 °C and 25 °C (Figure 2.32) the uniform temperature distribution and electrical potential field on the painted generator result in an order of magnitude higher power density of 205 μW cm^{-2}. (Figure 2.33)

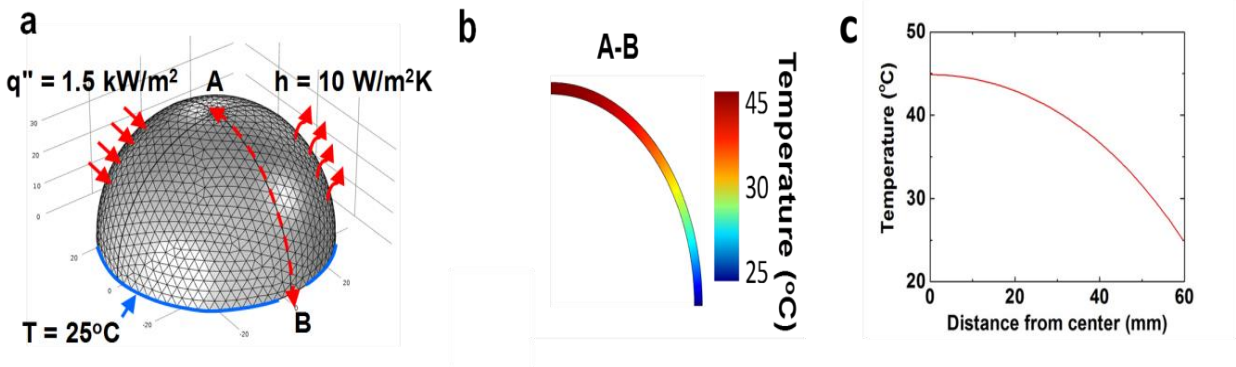

Fig. 2.32. A finite element model for a hemispherical heated substrate.

(**a**) A meshed substrate that is subject to a uniform heat flux of 1.5 kW/m^2, and natural convection (h = 10 W m^{-2} K^{-1}). The bottom surface is set at 25 °C. (**b, c**) Temperature distribution along an arc A-B. A and B indicates the apex and the bottom of an alumina hemisphere, respectively. Red arrows indicate the heat flux and blue arrows present the temperature on the bottom of hemisphere.

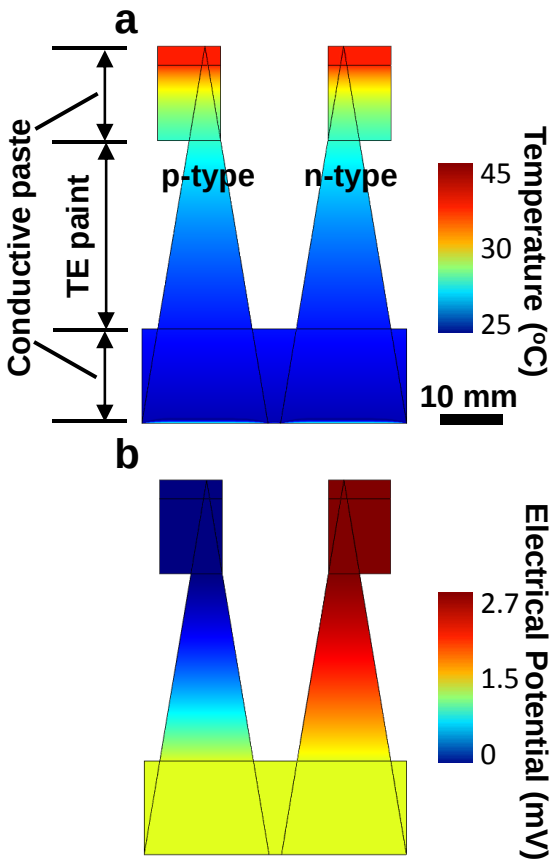

Fig. 2.33. Calculated (a) temperature and (b) electrical potential distribution of a pair of p- and n-types of painted TE generator.

2.4.2 Output characteristics of hemispherical thermoelectric devices

Figure 2.34 show output characteristics of painted hemispherical TE devices. Under temperature difference of 19.7°C, the output voltage was 18 mV and output power was 2.6 μW. A little lower output voltage than those of other devices could come from the deviation between actual temperatures applied to TE legs and temperatures at the hot and cold sides due to heat loss arising from small contact area of TE devices to the hot side. Lower output power was attributed to higher resistance and lower output voltage. Although this hemi-spherical TE device exhibited lower output power density due to large-sized TE layers, these results validate that TE painting process facilitated shape engineering of TE materials on any-shaped surfaces while maintaining their high TE performance, which should be the most effective heat energy collection from any heat sources.

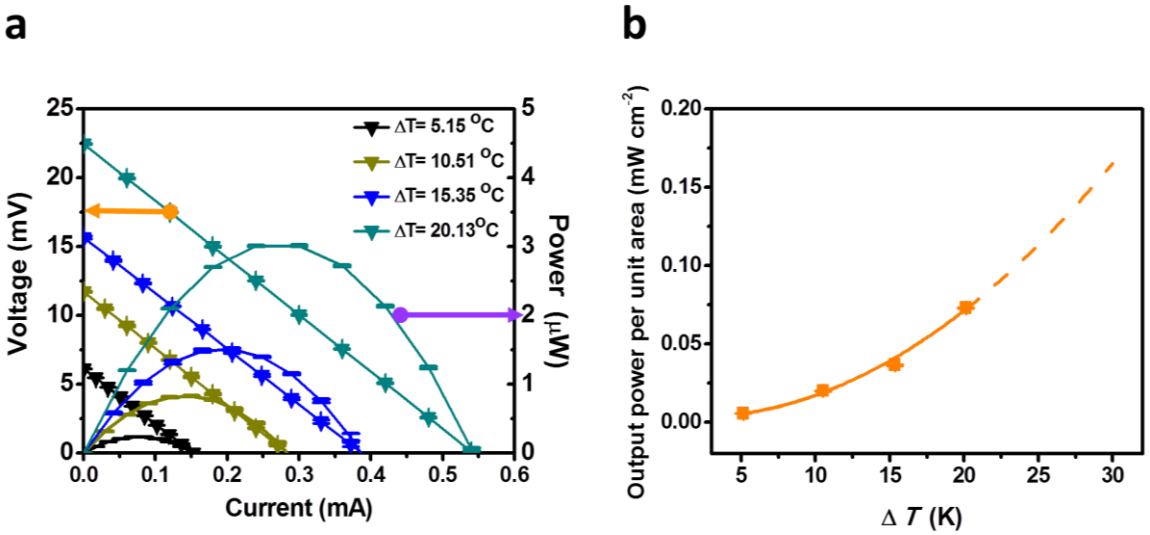

Fig. 2.34. Output characteristics of hemispherical TE devices

The output power density of the hemispherical generator was calculated with the assumption of same dimensions of TE legs with others. The fact that the output power density of the TE devices painted on flat and curved substrates with the same dimension of TE legs merges into the same line validates the applicability of the TE paints to any-shaped surfaces. (Figure 2.35)

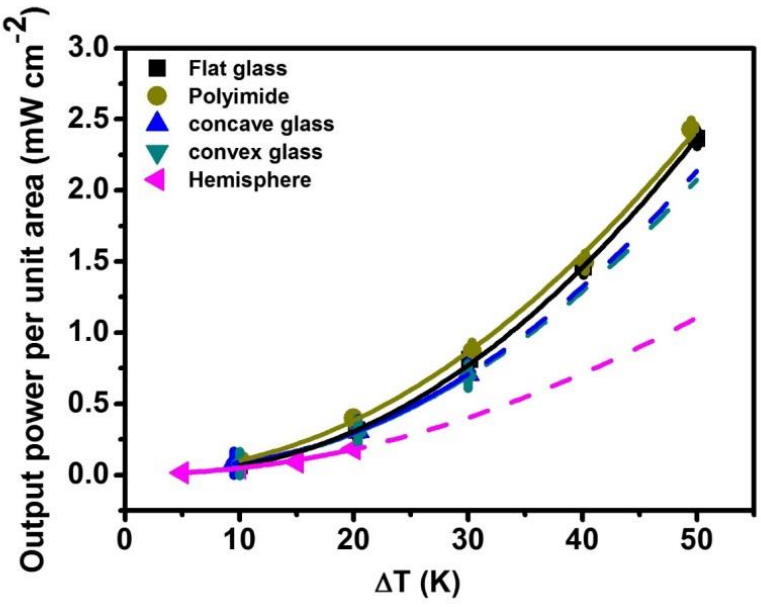

Figure. 2.35. Comparison of output power densities of painted TE devices

2.5 Fabrication of through-plane type thermoelectric device using molding process

In addition, the through-plane TE generator was fabricated using the molded disks prepared from the TE paints. The considerable sintering effects on TE paints function not only for 2D thick films in μm scale but also for 3D blocks in mm scale. For example, n- or p-type TE paints were added into ring-shaped molds and were dried, followed by annealing at 450 °C for 30 min (Figure 2.36a and b) with no external pressure, generating the robust TE ring. This ring-shape TE block can be directly utilized for cylindrical TE generators with radial heat transfer combined with the pipe heat exchangers[13]. Furthermore, disk-, square-, and triangle-shaped 3D blocks were obtained via using same shaped molds (Figure 2.36a and b). The SEM image in Figure 2.36c reveals well-connected dense grains that are very uniform in the scale of several hundred micrometers. In the control experiments without the ChaM, the microparticles remained just powdery as observed in painted materials. This successful molding process shows the versatility of our TE paints for designing TE materials in 3D as well as 2D.

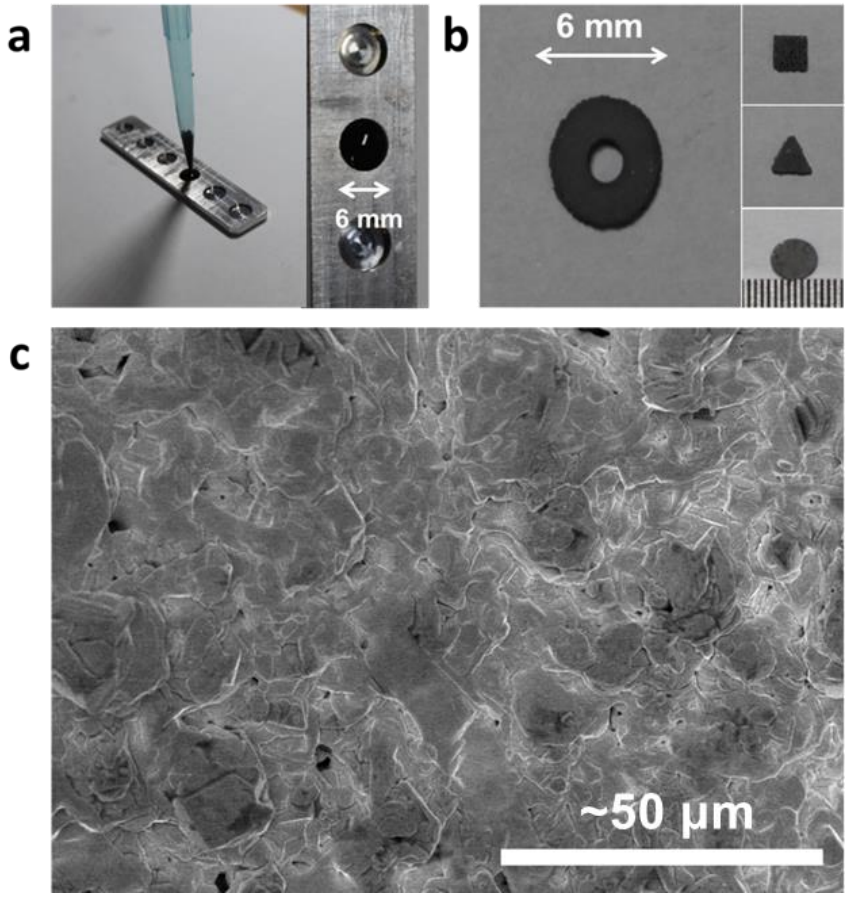

Fig. 2.36. Moulding process of TE paints. (**a**) A photograph showing TE molding process. (**b**) A photograph showing molded 3D blocks with diverse shape such as ring, cube, triangle, and disk. (**c**) SEM image of the molded sample.

2.5.1 The process of through-plane type thermoelectric device

Two pairs of n- and p-type molded disks with the diameter of 4.0 mm and thickness of 1.0 mm were assembled by soldering with a Bi-Sn solder to Cu foil electrodes on an alumina hemisphere (Figure 2.37). The top sides of TE disks were electrically interconnected with Cu foil electrodes by soldering, which produced the through-plane TE generator on a hemisphere. The internal resistance was as low as 0.014 Ω, comparable to that of the conventional module. (Figure 2.38)

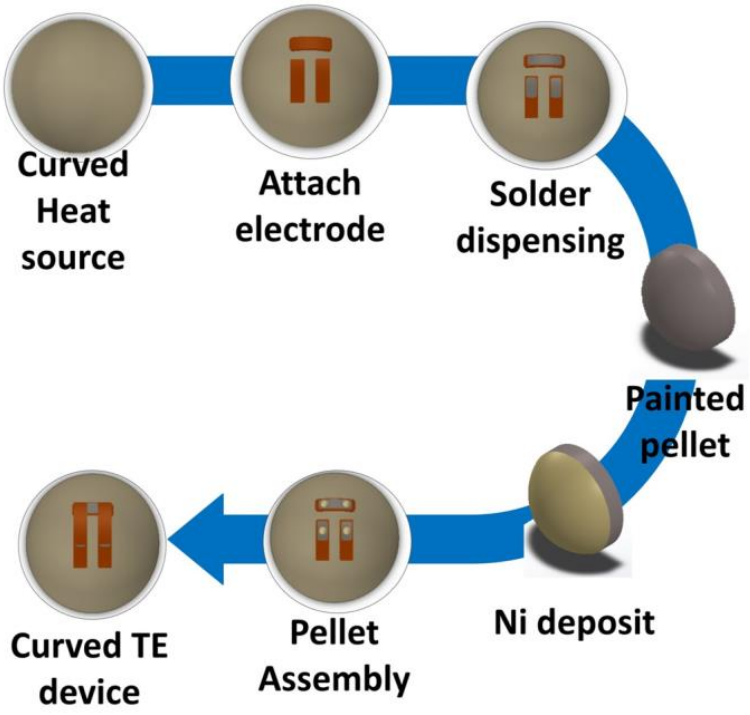

Fig. 2.37. Scheme for the fabrication of the TE generator.

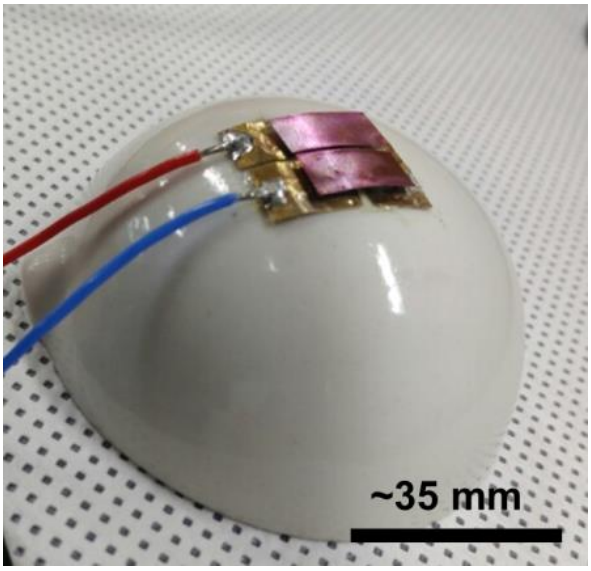

Fig. 2.38. A photograph of the fabricated TE generator.

2.5.2 Output voltage and power density of the through-plane thermoelectric device

Under the temperature difference of 14 ºC, this generator produced the voltage of 8.0 mV, output power of 1.1 mW, and output power density of 2.3 mW cm^{-2}. (Figure 2.39) Furthermore, the predicted power output density on the fitted function with the data points is about 26.3 mW cm^{-2} under the temperature difference of 50 ºC, which competes on a par with the conventional module[27]. These results clearly demonstrate the practicability of the painting technology in terms of the TE performance as well as the processability

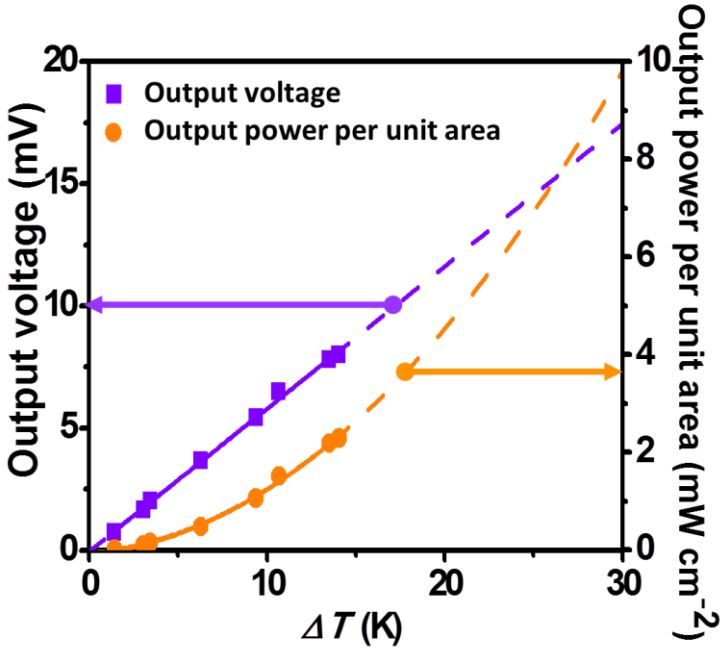

Fig. 2.39. Output voltage and output power density.

2.6 Experimental details

2.6.1 Synthesis of Bi_2Te_3-based inorganic thermoelectric paints.

To synthesize Sb_2Te_3-ChaM solution, elemental Sb (0.32 g) and Te (0.68 g) powder with stoichiometric ratio of Sb_2Te_4 were dissolved in mixed co-solvent including 0.20 mL of ethanethiol (97%) and 0.80 ml of ethylenediamine (>99.5%). After stirring for over 6 h, elemental Sb and Te were fully dissolved in solvent and the resulting solution showed a dark purple color. And 40 ml of acetonitrile was added into Sb_2Te_3-ChaM solution, followed by the centrifuge at 7500 RPM for 10min. After the centrifuge, the precipitated Sb_2Te_3- ChaM was added into mixed solvents including 3.6 g of glycerol and 0.40 g of ethylene glycol and it was sonicated for 10 min, which produced a dark brown-coloured solution. Bi_2Te_3 based TE powders were prepared by a mechanical alloying process. Typically, finely ground Bi, Sb, Te

and Se powder was weighed according to the stoichiometric ratios of $Bi_2Te_{2.7}Se_{0.3}$ (BTS) for a n-type paint and $Bi_{0.4}Sb_{1.6}Te_{3.0}$ (BST) for a p-type paint under N_2 atmosphere, and they were ball-milled with stainless steel balls including two balls with 0.5 inch in diameter and four balls with 0.25-inch in diameter for 4 h. The formation of BTS and BST alloys were confirmed by the XRD analysis. The sieving process was carried out at 45 μm to remove some agglomerated BTS or BST particles. 4 g of sieved TE powders were added into Sb_2Te_3- ChaM solution, followed by the sonication for 1 h, which produced black-coloured viscous TE paints. The viscosity and evaporation temperatures were adjusted by controllably varying the amount of glycerol and ethylene glycol.

2.6.2 Thermoelectric properties measurement

TE properties measurement were conducted on the samples prepared by repeated painting and drying of n-and p-type paints on aluminum plates, and subsequent annealing at 450 °C. The final samples were ~500 μm in thickness. To determine electrical conductivities at temperatures ranging from 27 °C to 127 °C, the sheet resistance of the samples was measured by a four-point Van der Pauw method (Keithley 2400 multimeter controlled Lab trace 2.0 software, Kiethley Instrument, Inc.) on a hot chuck plate. The four corners of the samples were contacted by sharp tips controlled by manipulators. The electrical conductivities were estimated with the thickness of the samples. To obtain the temperature-dependent Seebeck coefficients, the open circuit voltage and the temperature gradient were measured by two T-type thermocouples using a Keithley 2400 source-meter and a Keithley 2000 multi-meter. The measuring set-up lied on a hot-plates and the measuring temperatures were controlled by heating a hot-plate. To apply the temperature differences, applied powers of TE modules contacted with the samples was adjusted. Typically, 6 data points were obtained with the applied temperature differences at two points contacted by thermocouples across the sample ranging from ±1 °C to 5 °C. The Seebeck coefficient was calculated based on the slope of the voltage versus the temperature-difference curves. These set-up were confirmed by measuring the electrical conductivity and the Seebeck coefficient of n-type Bi_2Te_3 and p-type BiSbTe ingot samples, and the accuracy was within ±3%. We extracted The thermal conductivity was extracted by using the equation $\kappa = \rho C_p D$, where ρ is the density, C_P is the specific heat capacity, and D is the thermal diffusivity. The densities were measured by commercial equipment (BELPycno, microtracBEL). The specific heat capacities were calculated by assuming the law of mixture and by using the value of $Bi_{0.4}Sb_{1.6}Te_4$, Sb_2Te_3, Bi_2Te_3, and Bi_2Se_3. Thermal diffusivities were measured in a temperature range from 300 °C to 450 °C by using laser flash analysis (LFA 457, Netzsch). Carrier concentration and mobility were measured by a Hall measurement system (BIO-PAD, HL5500PC) at room temperature.

2.6.3 Measurement of TE power generation

Performance of TE power generator was investigated by measuring the I-V curve and the output power density under temperature differences across the devices using a home-built set-up. (Figure 3.1) In order to produce a reliable temperature difference ranging 5 °C to 50 °C across the TE devices, the hot side temperature was raised using a flat band heater, powered by a voltage converter. The cold side temperature was maintained at 20 ± 0.5 °C using a TE Peltier cooler. The temperature differences were measured by two T-type thermocouples that were in contact with hot and cold sides, by using Keithley 2000 multimeter. Two Ag electrodes in prepared TE generators were connected to Keithley 2400 source-meter and the I-V characteristics were measured by using Lab trace 2.0 software (Keithley Instrument, Inc) under desired temperature differences. The output power density (output power per unit area) was calculated with total cross-sectional areas of TE layers.

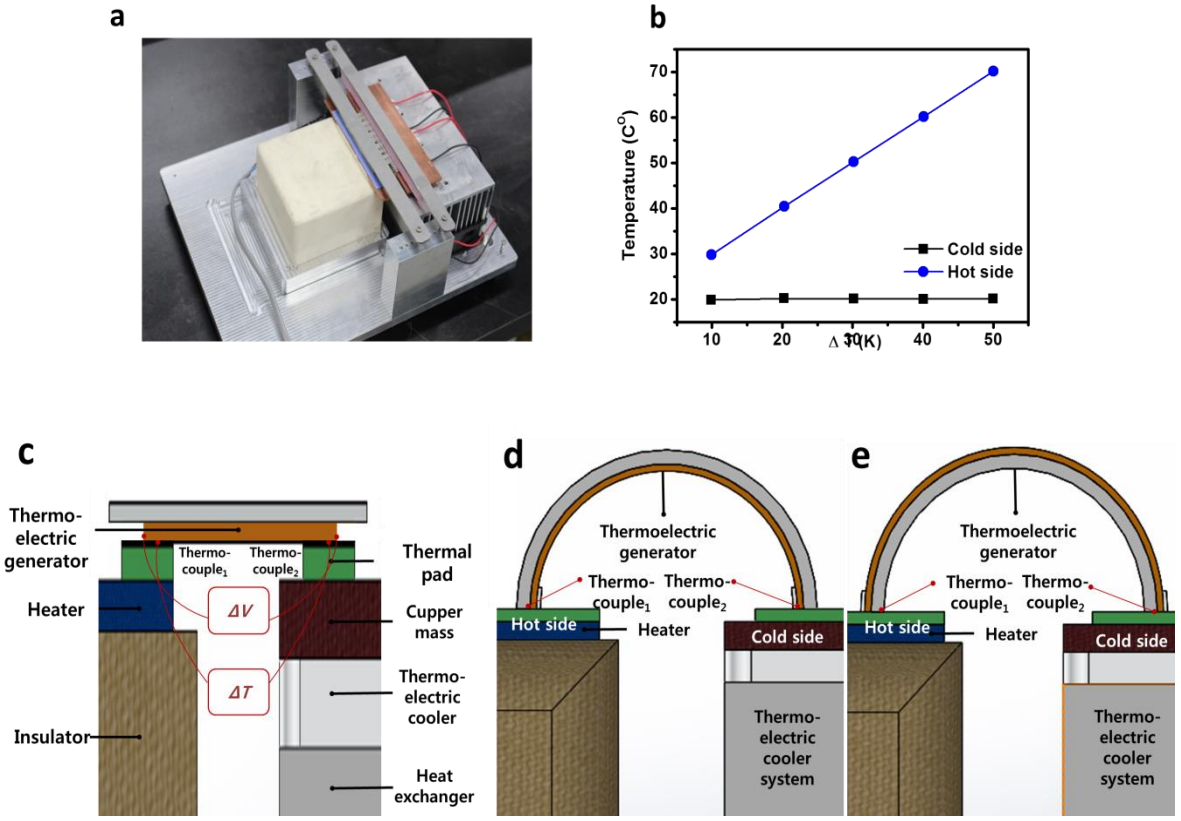

Figure 2.40. TE power measurement set-up. (**a**) A photograph of TE device power measurement system. (**b**) The temperature differences between the cold and hot sides. Schematic illustrations for measuring the power of TE devices on (**c**) a flat substrate, (**d**) on a concave substrate, and (**e**) on a convex substrate.

2.7 Conclusion

In summary, I report the first successful demonstration of the concept of TE painting using molecular Sb_2Te_3-ChaM assisted all-inorganic TE paints. Synthesized molecular Sb_2Te_3 based chalcogenidometalate acted as a solder for n-and p-type TE particles. This effect helped the bottom-up assembly of TE particles by interconnection of grains. It resulted in the huge densification and grain growth in TE particles upon heating, which led to the exceedingly high *ZT* values of 0.69 for n- and 1.15 for p-type in painted materials. Furthermore, the versatility of TE paints was applied to 2D painted films as well as 3D molded blocks, suggesting a new way of dimension- and shape-engineering TE materials. Especially, all-painted TE generators exhibiting exceedingly high output power density were fabricated on flat and curved surfaces such as hemi-cylinders and hemi-spheres. The current study not only unveil previously unknown process for engineering efficient TE materials, but it also makes a significant contribution to the basic understanding on the bottom-up assembly of inorganic semiconductor particles with molecular ChaMs. This approach enables extraordinarily high TE performance of shape- and dimension-engineered TE materials, opening new design spaces of TE materials and devices beyond conventional technologies. At the same time, TE painting provides facile and cost-effective way to fabricate efficient TE generators directly on any heat sources. I strongly believe that this approach will widely be extended to various electronic materials and devices for future technologies development such as 3D printed electronics and painted electronic artwork.

Parts of this chapter were published in the article “High-performance shape-engineerable thermoelectric painting” Nature Communications **2016, *7*, 13403.

References

1. Mitzi, D. B. Solution processing of chalcogenide semiconductors via dimensional reduction. *Adv. Mater.* **2009**, 21, 3141-3158.
2. Mitzi, D. B. Solution-processed inorganic semiconductors. *J. Mater. Chem.* **2004**, 14, 2355.
3. Mitzi, D. B., Kosbar, L. L., Murray, C. E., Copel, M. & Afzali, A. High-mobility ultrathin semiconducting films prepared by spin coating. *Nature* **2004**, 428, 299-303.
4. Mitzi, D. B., Copel, M. & Chey, S. J. Low-voltage transistor employing a high-mobility spin-coated chalcogenide semiconductor. *Adv. Mater.* **2005**, 17, 1285-1289.
5. Webber, D. H., Buckley, J. J., Antunez, P. D. & Brutchey, R. L. Facile dissolution of selenium and tellurium in a thiol–amine solvent mixture under ambient conditions. *Chem. Sci.* **2014**, 5, 2498.
6. Webber, D. H. & Brutchey, R. L. Alkahest for V_2VI_3 chalcogenides: dissolution of nine bulk semiconductors in a diamine-dithiol solvent mixture. *J. Am. Chem. Soc.* **2013**, 135, 15722-15725.
7. Cheng, H.-Y., Jong, C. A., Chung, R.-J., Chin, T.-S. & Huang, R.-T. Wet etching of $Ge_2Sb_2Te_5$ films and switching properties of resultant phase change memory cells. *Semicond. Sci. Technol.* **2005**, 20, 1111-1115.
8. Kovalenko, M. V. et al. Semiconductor nanocrystals functionalized with antimony telluride zintl ions for nanostructured thermoelectrics. J. Am. Chem. Soc. **2010**, 132, 6686–6695.
9. Jimenez, S. *et al.* Synthesis and thermoelectric performance of a p-type $Bi_{0.4}Sb_{1.6}Te_3$ material developed via mechanical alloying. *Energy Convers. Manage.* **87,** 868-873 (2014).
10. Liu, W.-S. *et al.* Thermoelectric property studies on Cu-doped n-type $Cu_xBi_2Te_{2.7}Se_{0.3}$ nanocomposites. *Adv. Energy Mater.* **2011**, 1, 577-587.
11. Delaizir, G. et al. A comparative study of spark plasma sintering (SPS), hot isostatic pressing (HIP) and microwaves sintering techniques on p-type Bi_2Te_3 thermoelectric properties. Mater. Res. Bull. **2012**, 47, 1954–1960.
12. Jo, W., Kim, D.-Y. & Hwang, N.-M. Effect of interface structure on the microstructural evolution of ceramics. J. Am. Ceram. Soc. **2006**, 89, 2369–2380.
13. 45. Kingery, W. D. Densification during sintering in the presence of a liquid phase. I. Theory. J. Appl. Phys. **1959**, 30, 301–306.
14. Yan, X. *et al.* Experimental studies on anisotropic thermoelectric properties and structures of n-type $Bi_2Te_{2.7}Se_{0.3}$. *Nano Lett.* **2010**, 10, 3373-3378.
15. Kim, S. I. *et al.* Thermoelectrics. Dense dislocation arrays embedded in grain boundaries for high-performance bulk thermoelectrics. *Science* **2015**, 348, 109-114.
16. Rowe, D. M. Thermoelectric Handbook (CRC Press, 1995).
17. Chiritescu, C., Mortensen, C., Cahill, D. G., Johnson, D. & Zschack, P. Lower limit to the lattice

thermal conductivity of nanostructured Bi2Te3-based materials. J. Appl. Phys. **2009,** 106, 073503.

18. Lee, H. et al. Effects of nanoscale porosity on thermoelectric properties of SiGe. J. Appl. Phys. **2010**, 107, 094308.
19. Landauer, R. Electrical transport and optical properties of inhomogeneous media. AIP Conf. Proc. **1978**, 40, 2.
20. Vineis, C. J., Shakouri, A., Majumdar, A. & Kanatzidis, M. G. Nanostructured thermoelectrics: big efficiency gains from small features. *Adv. Mater.* **2010**, 22, 3970-3980.
21. Sootsman, J. R., Chung, D. Y. & Kanatzidis, M. G. New and old concepts in thermoelectric materials. *Angew. Chem. Int. Ed.* **2009**, 48, 8616-8639.
22. Mun, H., Choi, S. M., Lee, K. H. & Kim, S. W. Boundary engineering for the thermoelectric performance of bulk alloys based on bismuth telluride. *ChemSusChem* **2015**, 8, 2312-2326.
23. Minnich, A. J., Dresselhaus, M. S., Ren, Z. F. & Chen, G. Bulk nanostructured thermoelectric materials: current research and future prospects. *Energy & Environ. Sci.* **2009**, **2,** 466.
24. Kim, S. J., We, J. H. & Cho, B. J. A wearable thermoelectric generator fabricated on a glass fabric. *Energy Environ. Sci.* **2014**, 7, 1959.
25. Gupta, R. P., Mccarty, R. & Sharp, J. Practical contact resistance measurement method for bulk Bi2Te3-based thermoelectric devices. J. Electron. Mater. **2014**, 43, 1608–1612.
26. Incropera, F. P. Fundamentals of Heat and Mass Transfer (Willey, 2011).
27. Rowe, D. M. & Min, G. Evaluation of thermoelectric modules for power generation. J. Power Sources **1998**, 73, 193–198.

Acknowledgement

어느덧 2년의 시간이 지나고 UNIST 생활을 마무리 할 시점이 왔습니다. 생각보다 시간이 너무 빠르게 지나간 듯해 너무나 아쉬운 마음이 가득합니다. 적지 않은 나이에 직장생활을 하던 중 학업을 다시 하겠다는 결정을 하기에 쉽지 않았습니다. 하지만 지금 돌이켜 보면 학업을 하기로 결정한 것은 매우 잘한 선택이 였다고 생각됩니다. 일단 실력적으로나 성품적으로 너무나 훌륭하신 손재성을 교수님을 만나 좋은 연구성과를 만들 수 있었고 좋은 랩원들을 만나서 평온히 학업을 마칠 수 있었기 때문입니다. 교수님께서 제자들을 너무나도 사랑하시고 학생들이 학자로서 양성될 수 있도록 최선의 환경을 만들어 주셨습니다. 사소한 일도 스스로 하는 것을 마다하지 않으셨고 같이 연구를 진행하는데 어려움이 있을 때 마다 항상 같이 토론하며 새로운 아이디어를 만들어 더 좋은 연구를 할 수 있게 도와 주셨습니다. 앞으로 항상 고마워 하는 마음을 가지며 지내도록 하겠습니다. 또 같이 2년 동안 생활을 한 승기와 형우한테도 고맙다는 말을 하고 싶습니다. 동기서로서 항상 같은 공간에서 공부와 실험했던 기억들은 아마 잊지 못할꺼야. 또한 랩 상민이 민석이 혜원이와 곧 우리 랩에 들어올 다휘, 승회, 성헌이도 고마워 ㅎㅎ~

또한 처음 UNIST에서 생활을 잘 수 있게 도와준 현도빈 박사님, 논문에 도움을 주신 조욱 교수님 최경진 교수님 감사드린다는 말 전해드리고 싶고 좋은 학교 좋은교수님을 만나게 해주신 김서영 대표님 이진영 전무님 감사합니다. 회사로 돌아가 배운것들을 적용할 수 있도록 최선을 다 하도록 하겠습니다.

마지막으로 사랑하는 엄마 아빠 누나 매형 항상 고맙고 엄마 지금은 많이 아프지만 곧 건강해 질 꺼라 믿고 항상 내가 응원할께. 엄마 사랑해~~~~~~